

www.acsami.org Research Article

# High-Affinity Extended Bisphosphonate-Based Coordination Polymers as Promising Candidates for Bone-Targeted Drug Delivery

Lesly Carmona-Sarabia, Gabriel Quiñones Vélez, Darilys Mojica-Vázquez, Andrea M. Escalera-Joy, Solimar Esteves-Vega, Esther A. Peterson-Peguero, and Vilmalí López-Mejías\*



Cite This: ACS Appl. Mater. Interfaces 2023, 15, 33397–33412



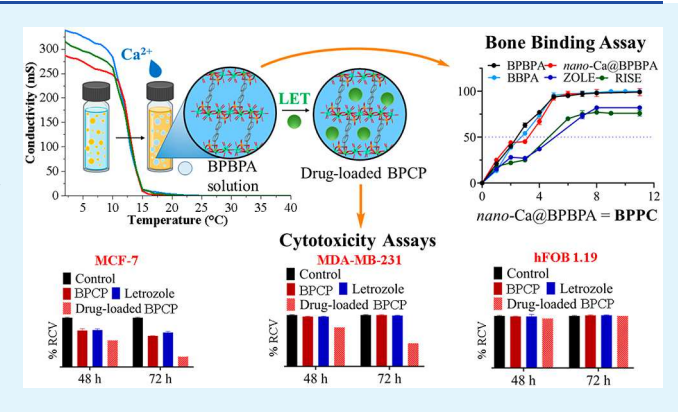
**ACCESS** I

III Metrics & More

Article Recommendations

Supporting Information

ABSTRACT: Extended bisphosphonate-based coordination polymers (BPCPs) were produced when 1,1'-biphenyl-4,4'-bisphosphonic acid (BPBPA), the analogue of 1,1'-biphenyl-4,4'-dicarboxylic acid (BPDC), reacted with bioactive metals ( $Ca^{2+}$ ,  $Zn^{2+}$ , and  $Mg^{2+}$ ). BPBPA-Ca (11 Å × 12 Å), BPBPA-Zn (10 Å × 13 Å), and BPBPA-Mg (8 Å × 11 Å) possess channels that allow the encapsulation of letrozole (LET), an antineoplastic drug that combined with BPs treats breast-cancer-induced osteolytic metastases (OM). Dissolution curves obtained in phosphate-buffered saline (PBS) and fasted-state simulated gastric fluid (FaSSGF) demonstrate the pH-dependent degradation of BPCPs. Specifically, the results show that the structure of BPBPA-Ca is preserved in PBS ( $\sim$ 10% release of BPBPA) and collapses in FaSSGF. Moreover, the phase inversion temperature nanoemulsion



method yielded nano-Ca@BPBPA (~160 d. nm), a material with measurably higher (>1.5x) binding to hydroxyapatite than commercial BPs. Furthermore, it was found that the amounts of LET encapsulated and released (~20 wt %) from BPBPA-Ca and nano-Ca@BPBPA are comparable to those of BPDC-based CPs [i.e., UiO-67-(NH<sub>2</sub>)<sub>2</sub>, BPDC-Zr, and bio-MOF-1], where other antineoplastic drugs have been loaded and released under similar conditions. Cell viability assays show that, at 12.5  $\mu$ M, the drug-loaded nano-Ca@BPBPA exhibits higher cytotoxicity against breast cancer cells MCF-7 and MDA-MB-231 [relative cell viability (% RCV) = 20 ± 1 and 45 ± 4%] compared with LET (%RCV = 70 ± 1 and 99 ± 1%). At this concentration, no significant cytotoxicity was found for the hFOB 1.19 cells treated with drug-loaded nano-Ca@BPBPA and LET (%RCV = 100 ± 1%). Collectively, these results demonstrate the potential of nano-Ca@BPCPs as promising drug-delivery systems to treat OM or other bone-related diseases because these present measurably higher affinity, allowing bone-targeted drug delivery under acidic environments and effecting cytotoxicity on estrogen receptor-positive and triple-negative breast cancer cell lines known to induce bone metastases, without significantly affecting normal osteoblasts at the metastatic site.

KEYWORDS: coordination polymers, extended bisphosphonates, targeted drug delivery, pH-dependent degradation, bone affinity

## ■ INTRODUCTION

Breast cancer has become one of the most frequent cancers detected in patients, particularly women. The majority of the diagnoses (70–80%) for breast cancer express estrogen (ERpositive) or progesterone (PR-positive) receptors on breast neoplasm cells. When breast cancer grows independently from estrogen or progesterone receptors, it is classified as triple-negative breast cancer (TNBC). For these neoplasms, the bone is the principal site of metastases. So Both ERpositive and TNBC can induce bone metastases generating bone loss, leading to osteolytic metastases (OM). Treatments for OM are based on chemotherapy, radiotherapy, radiology, hormone therapy, or bone target agents. The main bone target agents employed to treat OM include antiresorptive agents such as bisphosphonates (BPs). BPs are analogues of pyrophosphates (P-O-P), which contain a P-C-P

backbone that promotes their binding to Ca<sup>2+</sup> ions without undergoing hydrolysis. When present, a hydroxyl group in the geminal carbon [P-C(OH)-P] allows BPs to increase their binding to the bone. BPs can inhibit bone resorption, increase bone mineral density, and interrupt the activity of the cancerous cells, thus reducing tumor growth. Pamidronic, alendronic (ALEN), zoledronic (ZOLE), and risedronic (RISE) acids are commercial BPs employed to treat OM. BPs are poorly absorbed; only 1–10% of the administered

Received: April 16, 2023 Accepted: June 13, 2023 Published: July 5, 2023





drug can reach the systemic circulation.<sup>8,10</sup> Treatments involving BPs usually require high doses, leading to severe side effects; these disadvantages limit the use of BPs to treat breast-cancer-induced OM.<sup>8-10</sup>

Drug-delivery systems (DDSs) can be used to reduce the side effects, provide controlled release, and selectively target cancer-related diseases. 11-14 Metal-organic frameworks (MOFs) have become promising candidates as DDSs due to their well-defined structures, tunable pore size, high surface area, high loading/release of guest compounds, amphiphilic internal microenvironment, and pH-dependent degradation under simulated physiological conditions. 13-18 For example, the organic ligand 1,1'-biphenyl-4,4'-dicarboxylic acid (BPDC) has produced various porous frameworks: UiO-67 (Zr), UiO-67-(NH<sub>2</sub>)<sub>2</sub> (Zr), bio-MOF-1 (Zn), and BPDC-Zr. 11,12,18-20 These materials have been employed as carriers for the intracellular delivery of chemotherapeutic agents such as pemetrexed, 5-fluorouracil (5-FU), and Ru-90, and other pharmaceutical compounds such as brimonidine, calcein, and  $\alpha$ -cyano-4-hydroxycinnamic acid. Specifically, 5-FU (~6 wt %) and pemetrexed (~18 wt %) were simultaneously loaded into UiO-67-(NH<sub>2</sub>)<sub>2</sub>; this MOF showed a pHdependent release of both drugs in simulated physiological buffers. 18 In addition, commercial BPs were employed recently to generate ALEN-, ZOLE-, and RISE-based coordination complexes and demonstrated suitable pH-dependent degradation, bone affinity [e.g., nano-Ca@ZOLE to hydroxyapatite (HA), 36%, 1 day], and cytotoxicity [e.g., nano-Ca@ALEN, relative cell viability (%RCV) =  $38 \pm 1\%$  at 7.5  $\mu$ M in 72 h] against the MDA-MB-231 cell line. However, these BPbased coordination complexes did not lead to porous materials able to encapsulate guest molecules. 21-23 Furthermore, the reaction of benzene-1,4-bis(bisphosphonic acid) (BBPA), the BP analogue of benzene-1,4-dicarboxylic acid (BDC), coordinated with Ca2+ successfully led to BBPA-Ca form I, a 3D framework with channels (7  $\times$  12 Å) large enough to encapsulate and release 5-FU (~30 wt %).24 From this perspective, it was hypothesized that the synthesis of the BP analogue of BPDC would allow the design of network coordination polymers comparable to UiO-67 (Zr), UiO-67-(NH<sub>2</sub>)<sub>2</sub> (Zr), bio-MOF-1 (Zn), and BPDC-Zr, offering similar drug loading and release with the potential for bone-targeted drug delivery of antineoplastic drugs under acidic environments to the metastatic site, the bone.

In this work, the organic ligand 1,1'-biphenyl-4,4'-bisphosphonic acid (BPBPA) was synthesized and coordinated with three nontoxic metals (Ca2+, Zn2+, and Mg2+) to achieve porous extended BPBPA-based coordination polymers (BPBPA-based BPCPs) for the first time. The resulting materials were designed to bind to the bone microenvironment because these contain structural features such as the P-C-P backbone and the geminal hydroxyl group [P-C(OH)-P], which are known to impart affinity in BPs to calcium ions. The three nontoxic metals (Ca2+, Zn2+, and Mg2+) were selected due to their role in physiological processes, specifically osteoblastic bone formation. 25-27 This work is intended to report on the design of a new class of 3D extended BPCPs as promising bone-targeting DDSs, which would enable their future use in the treatment of breast-cancer-induced OM and other bone-related diseases.

#### EXPERIMENTAL SECTION

- 1. Synthesis of BPBPA. The synthesis of BPBPA has not been previously reported. Therefore, the Lecouvey reaction, commonly employed to produce commercial or aromatic BPs, was adapted to generate this organic ligand.<sup>28-31</sup> About 1.0 g of 1,1'-biphenyl-4,4'dicarbonyl dichloride (BPDCl) was added to 7 mL of tris-(trimethylsilyl) phosphite (TMSP) at 0 °C. The reaction was left at room temperature for 1 h and then for 3 days at 50 °C. After this period, the excess of TMSP was removed by rotoevaporation. Subsequently, methanol was added, and the reaction mixture was left under continuous stirring for 1 day. The excess solvents were removed by rotoevaporation. The product was characterized by nuclear magnetic resonance (NMR), Raman spectroscopy, powder X-ray diffraction (PXRD), differential scanning calorimetry (DSC), and thermogravimetric analysis (TGA), which confirmed its identity and purity. A complete description for the synthesis of BPBPA is provided in the Supporting Information (SI).
- 2. Synthesis of BPBPA-Based BPCPs. Solutions of BPBPA (0.01 mmol) and the corresponding salts Ca(NO<sub>3</sub>)<sub>2</sub>4H<sub>2</sub>O (0.01 mmol), Zn(NO<sub>3</sub>)<sub>2</sub>6H<sub>2</sub>O (0.01 mmol), and Mg(NO<sub>3</sub>)<sub>2</sub>6H<sub>2</sub>O (0.01 mmol) were prepared separately. For this experiment, ~ 10 mg BPBPA was placed in a 20 mL scintillation vial and dissolved in 10 mL of nanopure water. Subsequently, the metal salt solutions were prepared in individual 20 mL scintillation vials by dissolving 4.20 mg of Ca(NO<sub>3</sub>)<sub>2</sub>·4H<sub>2</sub>O, 6.0 mg of Zn(NO<sub>3</sub>)<sub>2</sub>·6H<sub>2</sub>O, and 4.85 mg of Mg(NO<sub>3</sub>)<sub>2</sub>·6H<sub>2</sub>O in 10 mL of nanopure water. Later, 5.0 mL of each of the previously prepared solutions (BPBPA solution + metal salt solution) was transferred to individual 20 mL vials. These mixtures were left in a heating block for 1 day at 70 °C. When crystals were visually detected, the vials were removed from the heating block and left undisturbed at room temperature. The crystals obtained through this procedure were collected via vacuum filtration. Individual descriptions of these experimental procedures are provided in the SI.
- 3. Characterization of BPBPA and BPBPA-Based BPCPs. NMR of BPBPA. <sup>1</sup>H, <sup>13</sup>C-APT, and <sup>31</sup>P NMR were recorded by employing a Bruker Ascend Aeon 700 MHz NMR spectrometer. The instrument was equipped with variable temperature and crosspolarization magnetic angle spinning. The solute was dissolved in deuterium oxide, and the experiment was performed at room temperature. TopSpin (version 3.5) was used to analyze the data collected.

Raman Vibrational Spectroscopy. A Thermo Scientific DXR Raman microscope was employed to collect the Raman spectra of BPBPA, BPBPA-Ca, BPBPA-Zn, and BPBPA-Mg. A total of 32 scans each with an exposure time of 5 s were collected between 3500 to 250 cm<sup>-1</sup>, as described in the SI.

PXRD. A Rigaku XtaLAB SuperNova X-ray diffractometer equipped with a microfocus Cu K $\alpha$  radiation ( $\lambda$  = 1.5417 Å) source and a HyPix3000 X-ray detector was utilized to record the PXRD patterns of BPBPA and the BPBPA-based BPCPs. The experiment was performed at 300 K, employing a  $2\theta$  range from  $6^{\circ}$  to  $60^{\circ}$  in fast  $\Phi$ mode for 90 s, as described in the SI.

DSC. A DSC Q2000 calorimeter (TA Instruments Inc.) equipped with a 50-position autosampler and a refrigerated cooling system (RCS40) was used to determine the average melting point of BPBPA, as described in the SI.

TGA. A TGA Q500 analyzer (TA Instruments Inc.) was employed to record the TGA thermographs of BPBPA, BPBPA-Ca, BPBPA-Zn, and BPBPA-Mg. The experiment was carried out from 25 to 600 °C under N2 (60 mL/min) at a heating rate of 5 °C/min, as described in

Single-Crystal X-ray Diffraction (SCXRD). Single crystals of BPBPA-Ca and BPBPA-Zn were examined under a Nikon Eclipse Microscope LV100N POL instrument to observe their crystal quality. Adequate single crystals of BPBPA-Ca and BPBPA-Zn were mounted in MiTeGen microloops with paratone oil. Data collection for BPBPA-Ca and BPBPA-Zn was performed in a Rigaku XtalLAB SuperNova single microfocus diffractometer equipped with a

HyPix3000 X-ray detector (*CrysAlisPro* software vs 1.171.39.45c) at 100 K.

The crystals of BPBPA-Mg were too small to collect reliable crystallographic data in a conventional X-ray diffractometer. Therefore, ~10-15 mg of this material was sent to the National Science Foundation (NSF)'s ChemMatCARS, at Sector 15, of the Advanced Photon Source (APS), Argonne National Laboratory (ANL). Synchrotron measurements of BPBPA-Mg were recorded using a Huber three-circle diffractometer. The instrument was equipped with a Pilatus 3X 1 M CdTe detector and an Oxford cryojet. The experiment was performed with the  $\omega$  angle at  $-180^{\circ}$ , the  $\kappa$  angle at  $0^{\circ}$  and  $30^{\circ}$ , and the  $\varphi$  angle scanned over the range of  $360^{\circ}$ . Data integration was performed in Bruker APEX 3 software. The data reduction was performed in the SAINT, version 8.38A, and SADABS, version 2016, programs. The experiments were performed at 273 K. Elucidation of these structures was performed using full-matrix leastsquares (F<sup>2</sup> mode) and direct methods in OLEX2 software, version 1.2. Crystallographic data collection and analysis are discussed in the

Scanning Electron Microscopy (SEM)—Energy-Dispersive Spectroscopy (EDS). The SEM micrographs and X-ray elemental analysis of BPBPA-Ca, BPBPA-Zn, and BPBPA-Mg were recorded by using a JEOL JSM-6480LV scanning electron microscope. The instrument was equipped with Everhart—Thomley secondary electron imaging and energy-dispersive X-ray analysis Genesis 2000 detectors. For imaging, powdered samples of BPBPA-Ca, BPBPA-Zn, and BPBPA-Mg were coated with gold by using a PELCO SC-7 auto sputter coater and a PELCO FTM-2 film thickness monitor for 10 s. The SEM—EDS images of the BPBPA-based BPCPs were collected as described in the SI.

- **4. Dissolution in Simulated Physiological Buffers.** About 100.0 mL of phosphate-buffered saline (PBS) or fasted-state simulated gastric fluid (FaSSGF) was separately transferred to a 250 mL beaker; these solutions were left under stirring at 37 °C (150 rpm). About 15.0 mg of powdered BPBPA-based BPCPs was separately added to the PBS or FaSSGF buffered solutions. At selected time points (0, 1, 3, 6, 24, 48, and 72 h), 1 mL aliquots were taken out and diluted to a final volume of 5 mL in a volumetric flask. Subsequently, the absorbance of BPBPA released from the BPBPA-based BPCPs was evaluated at  $\lambda_{\text{max}} = 275$  nm (PBS) or  $\lambda_{\text{max}} = 266$  nm (FaSSGF), employing a Cary 100 spectrophotometer (Agilent UV Cary Scan version 20.0.470). The dissolution curve of BPBPA was assessed as a control group. The dissolution experiments were performed in duplicate for each BPBPA-based BPCP in PBS and FaSSGF, using adapted methods,  $^{21-24}$  which are described in the SI.
- **5. Synthesis of** *nano*-Ca@BPBPA. The synthesis of *nano*-Ca@BPBPA was performed in a Crystalline (Technobis, Crystallization Systems, Alkmaar, The Netherlands) using adapted procedures. <sup>21–24</sup> Determination of the phase inversion temperature (PIT) and the PIT-nanoemulsion method for this system is described in the SI. Dynamic light scattering (DLS) measurements were performed to determine the particle size distribution and polydispersity of *nano*-Ca@BPBPA in the supernatant from the aqueous phase. Furthermore, the particle size distribution and polydispersity of *nano*-Ca@BPBPA were evaluated in 10% fetal bovine serum (FBS)/PBS after 0, 24, and 48 h to determine the aggregation of this material in a simulated physiological dispersant. All DLS measurements were performed in a Malvern Panalytical Zetasizer NanoZS, as described in the SI.
- **6. Binding Affinity Assays.** Binding assays were conducted by employing HA to assess the affinity of BPBPA and *nano*-Ca@BPBPA to the bone. All experimental and control groups were left under constant stirring (150 rpm) for 0–12 days at 37 °C in PBS. The binding of BPBPA and *nano*-Ca@BPBPA was determined using adapted procedures. An an encourage BPBPA, *nano*-Ca@BPBPA, HA, a physical mixture (1:1) of HA/*nano*-Ca@BPBPA, HA-BPBPA, and HA-*nano*-Ca@BPBPA were characterized by SEM–EDS and PXRD. Binding assays are described in the SI.
- **7. Drug Loading and Release.** *Drug Loading into BPBPA-Ca.* The loading of letrozole (LET) into BPBPA-Ca was performed by employing ethanol as the solvent. For this procedure, 20 mg of

BPBPA-Ca, 7 mg of LET, and 1 mL of ethanol were placed in a 1.5-mL vial. Subsequently,  $\sim\!\!7$  mg of LET was additionally added, and the vial was left undisturbed at 50 °C for 24 h to allow the loading of LET into BPBPA-Ca. At the same conditions,  $\sim\!\!20$  mg of BPBPA-Ca and 7 mg of LET in 1 mL of ethanol were prepared separately as control groups. The drug-loaded BPBPA-Ca (experimental), BPBPA-Ca (control), and LET (control) were characterized by EDS, TGA, and PXRD.

Drug Loading into nano-Ca@BPBPA. The PIT-nanoemulsion method was also utilized to load LET into nano-Ca@BPBPA. First nano-Ca@BPBPA was synthesized, then a LET solution was added, and the system was left under stirring (1,250 rpm) for 1 h at 80 °C, allowing the loading of LET into nano-Ca@BPBPA. Both nano-Ca@BPBPA and drug-loaded nano-Ca@BPBPA were characterized by EDS, TGA, and PXRD.

Release from Drug-Loaded BPBPA-Ca. About 100 mL of FaSSGF was placed in a 250-mL beaker and left in constant stirring at 37 °C (150 rpm). To record the first time point (0 h), an aliquot (1 mL) was taken out before addition of the drug-loaded BPBPA-Ca. Subsequently, about 20 mg of powdered drug-loaded BPBPA-Ca (experimental) was placed in the FaSSGF solution. At each time point (0, 1, 3, 6, 24, 48, and 72 h), an aliquot (1 mL) was taken out and diluted to a final volume of 5 mL in a volumetric flask. The absorbance of each dilution was measured at  $\lambda_{\rm max}=238$  nm to determine the amount (%) of LET released from BPBPA-Ca. The released curve of LET (control) in FaSSGF was determined for comparison. This experiment was performed in duplicate.

**8. Cell Viability Assays.** *Cell Culture Methods.* Human breast cancer (MCF-7 and MDA-MB-231) and osteoblast-like (hFOB 1.19) cell lines were incubated by employing Dulbecco's modified Eagle medium (DMEM) (37 °C) and DMEM/F12 (34 °C) media, respectively, in 5% CO<sub>2</sub>. Cell lines were supplemented using 10% FBS, and 1% Pen-Strep and medium exchange were performed twice a week. Cell passages were carried out at 80% confluence.

Cell Viability Assays. Cell lines were seeded in 96-well plates at a density of  $5 \times 10^3$  cells/mL and incubated for 24 h before treatment, allowing cells to be attached to the plate. Both cell lines were treated with 100  $\mu$ L/well with 2-fold serial dilutions of BPBPA (0–400  $\mu$ M) and LET  $(0-200 \mu M)$  to determine the half-maximal inhibitory concentration (IC<sub>50</sub>) for the MCF-7, MDA-MB-231, and hFOB 1.19 cell lines treated with BPBPA and LET after 24, 48, and 72 h. The cell lines were also treated with LET, empty, and drug-loaded nano-Ca@ BPBPA (0-50  $\mu$ M) to assess the relative cell viability (%RCV) under the same conditions employed for the IC50. Cell viability assays were performed after 24, 48, and 72 h of treatment. Control groups were treated with media (DMEM or DMEM/F12) supplemented with 1% Pen-Strep. At each time point, the media were exchanged with 100  $\mu$ L of 10% alamarBlue cell viability reagent, and the 96-well plates were incubated for 4 h. The fluorescence was determined at  $\lambda_{\text{ext}} = 560$  and  $\lambda_{\rm em}$  = 590 nm. The IC<sub>50</sub> was determined for BPBPA and LET after generating dose-response curves (% cell live vs concentration) using GraphPad Prism, version 9.3.0, with the nonlinear regression function. The metabolically active cells (i.e., % cells that are proliferating) were evaluated by comparing the percentage of live cells of the control groups with the cells treated with LET, empty, and drug-loaded nano-Ca@BPBPA to assess the relative cell viability (%RCV) at the same conditions as those employed for the IC50. All experiments were performed in triplicate, reporting the mean, standard deviation, and coefficient variation (%CV). The IC<sub>50</sub> curves of MCF-7, MDA-MB-231, and hFOB 1.19 cells treated with BPBPA and LET are presented in the SI.

## ■ RESULTS AND DISCUSSION

**Synthesis and Characterization of BPBPA.** The Lecouvey reaction, a well-established synthetic scheme used to obtain commercial BPs (ALEN, ZOLE, and RISE) and extended BPs such as BBPA, <sup>28–31</sup> was employed to generate the organic ligand BPBPA subsequently used to obtain extended BPBPA-based BPCPs. In the first step of the

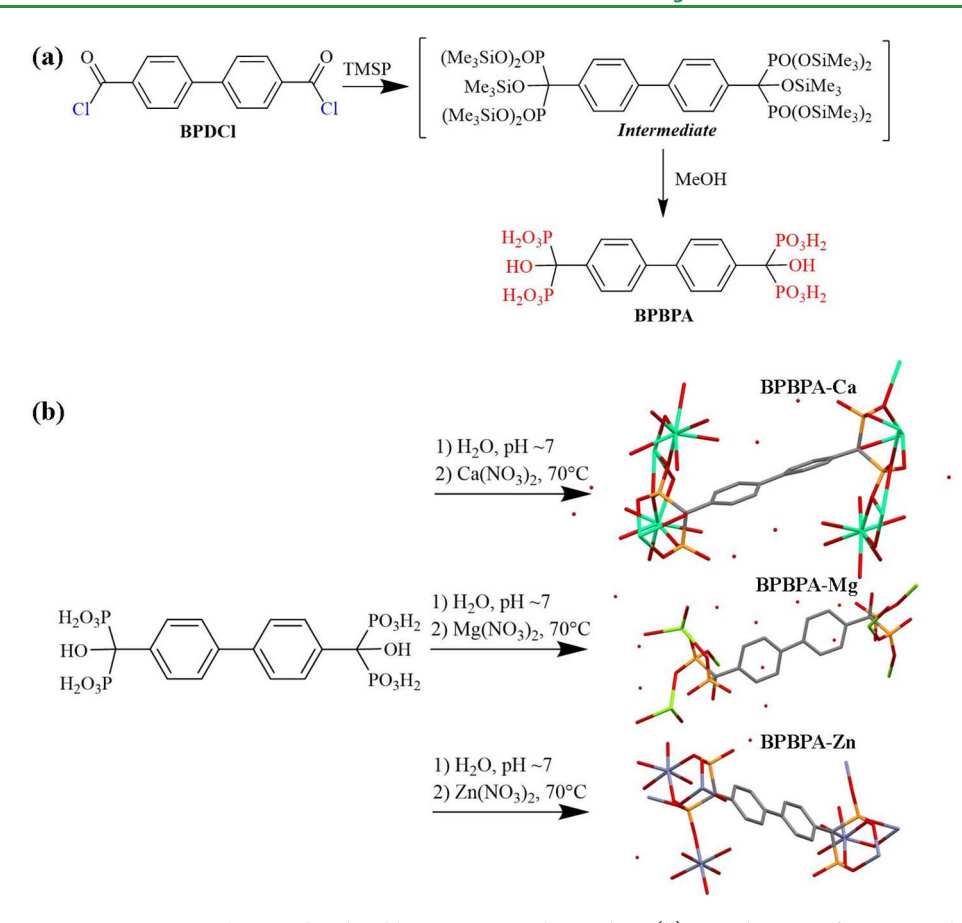


Figure 1. (a) Lecouvey reaction starting with BPDCl and yielding BPBPA as the product. (b) Coordination of BPBPA with three nontoxic metals  $(Ca^{2+}, Mg^{2+}, and Zn^{2+})$  yielding BPBPA-Ca, BPBPA-Mg, and BPBPA-Zn, respectively. The asymmetric units of BPBPA-Ca (Z' = 1), BPBPA-Zn (Z' = 0.5, extended), and BPBPA-Mg (Z' = 1) are displayed as products for each reaction. Hydrogen atoms in the ligand and coordinated and uncoordinated water molecules were omitted for clarity.

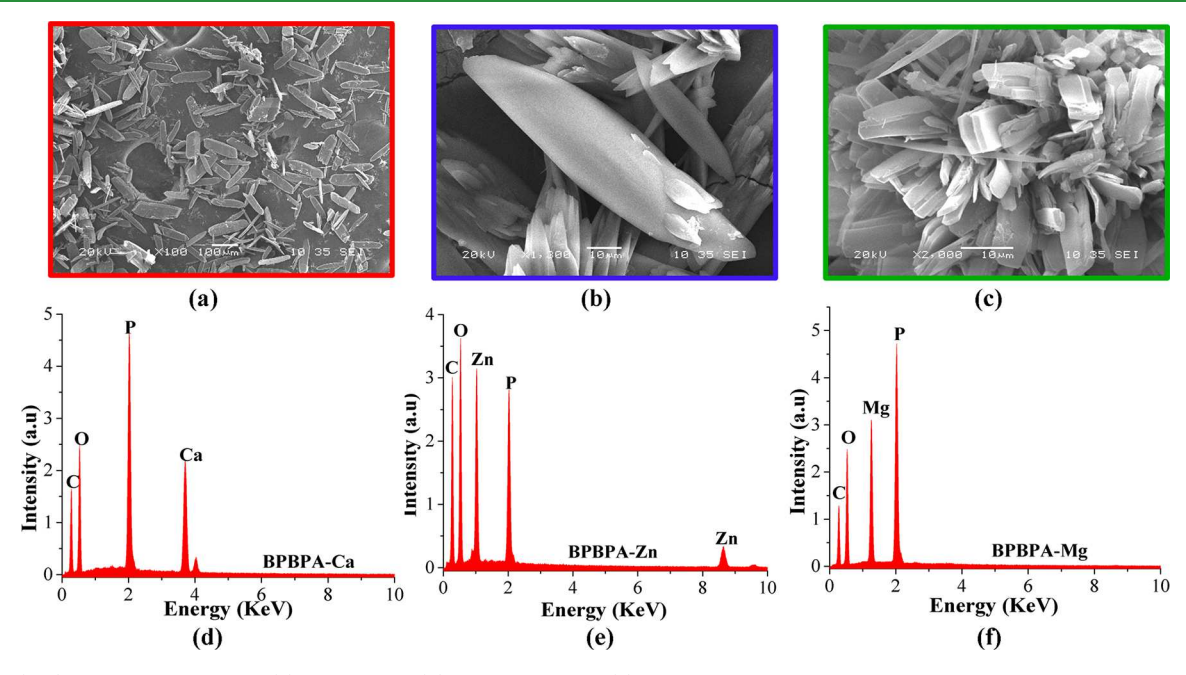


Figure 2. (top) SEM micrographs of (a) BPBPA-Ca, (b) BPBPA-Zn, and (c) BPBPA-Mg. All SEM micrographs were recorded by employing a 5-nm-thick layer of gold. (bottom) Elements such as carbon, oxygen, phosphorus, calcium, zinc, and magnesium were detected by EDS analysis of (d) BPBPA-Ca, (e) BPBPA-Zn, and (f) BPBPA-Mg.

Lecouvey reaction, BPDCl was utilized as the starting material, yielding an ester intermediate in the presence of TMSP. This

intermediate was hydrolyzed in methanol, leading to the formation of the desired organic ligand, BPBPA (~90% yield;

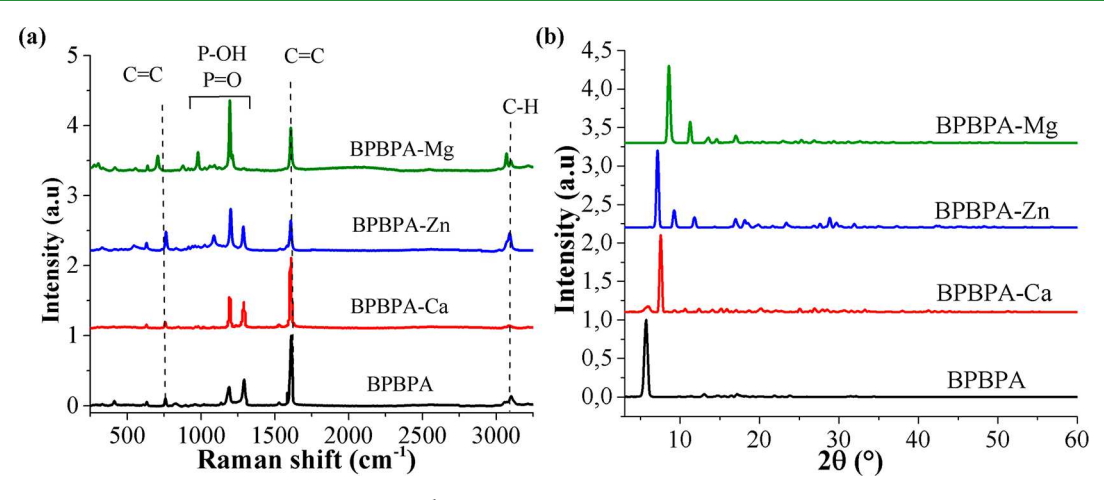


Figure 3. (a) Raman spectra in the region 3500 to 250 cm $^{-1}$  and (b) diffraction patterns for BPBPA (black), BPBPA-Ca (red), BPBPA-Zn (blue), and BPBPA-Mg (green). The PXRD patterns were collected at 300 K in fast  $\Phi$  mode using a 90 s exposure.

Table 1. Summary of the Crystallographic Parameters for BPBPA-Ca, BPBPA-Zn, and BPBPA-Mg<sup>a</sup>

	BPBPA-Ca	BPBPA-Zn	BPBPA-Mg
empirical formula	$[Ca_3(C_{14}H_8O_{14}P_4)(6H_2O)]\cdot 7H_2O$	$[Zn_3(C_{14}H_8O_{14}P_4)(4H_2O)]\cdot 4H_2O$	$[Mg_3(C_{14}H_8O_{14}P_4)(6H_2O)]\cdot 7H_2O$
fw (g/mol)	876.57	862.37	817.11
space group	$P\overline{1}$	$P\overline{1}$	$P\overline{1}$
temperature (K)	100(1)	139(4)	292(2)
λ (Å)	1.54184	1.54184	1.54184
a (Å)	10.9829(2)	5.4039(4)	10.9782(14)
b (Å)	11.8825(2)	9.6464(8)	11.5790(15)
c (Å)	13.0827(2)	12.2483(9)	12.9417(6)
α (deg)	87.510(1)	88.190(7)	90.357(2)
$\beta$ (deg)	76.716(1)	88.742(6)	103.814(2)
γ (deg)	78.678(1)	85.889(7)	104.686(2)
$V(Å^3)$	1629.33(5)	636.40(9)	1541.4(4)
Z	2	1	2
Z'	1	0.5	1
$ ho_{ m calc}~({ m g/cm^3})$	1.795	2.255	1.752
R <sub>p</sub>	0.0570	0.0627	0.0999
$R_{\rm wp}$	0.1675	0.1891	0.3314

<sup>&</sup>lt;sup>a</sup>Abbreviations:  $\lambda$  (X-ray source wavelength, Å), a/b/c (unit cell lengths, Å),  $\alpha/\beta/\gamma$  (unit cell angles, deg), V (unit cell volume, ų), Z (number of formula units per unit cell),  $\rho_{\text{calc}}$  (unit cell calculated density,  $g/\text{cm}^3$ ),  $R_p$  (R factor, %), and  $R_{\text{wp}}$  (weighted R factor,%).

Figure 1a). To the best of our knowledge, this is the first time the synthesis and characterization of BPBPA is reported in the literature. Characterization of the product by NMR, Raman spectroscopy, PXRD, TGA, and DSC confirmed the identity and purity of BPBPA (see the SI).

Synthesis and Characterization of the BPBPA-Based BPCPs. Three distinctive crystalline phases of the BPBPA-based BPCPs, namely, BPBPA-Ca, BPBPA-Zn, and BPBPA-Mg (Figure 1b), were obtained by exploring conditions such as the  $M^{2+}$ /BPBPA molar ratio (1:1 and 2:1), pH (6.0–8.0), and temperature (60–80 °C). From all of the conditions tested, it was observed that using a 1:1 molar ratio and neutral pH (~7.0, adjusted with 0.1 M NaOH) and at 70 °C led to the best conditions in terms of yield and crystal quality, particularly for BPBPA-Ca. SEM micrographs (Figure 2a–c) showed crystals (100–500  $\mu$ m) with a prismatic habit. EDS analysis confirmed the elemental composition of the BPBPA-based BPCPs (Figure 2d–f). Only these three solid forms were generated (no other phases could be identified).

Characteristic Raman spectra and diffraction patterns of the BPBPA-based BPCPs are shown in Figure 3. These results

confirm that three distinctive crystalline phases have been produced. Overlay of the diffraction patterns indicates that the crystal phases of the BPBPA-based BPCPs are not isostructural to those of the BBPA-based BPCPs. <sup>24</sup> A detailed description of the conditions employed for the synthesis and characterization of the BPBPA-based BPCPs is given in the SI.

The crystal structures of the BPBPA-based BPCPs were solved by employing direct methods and resulted in the crystallography parameters listed in Table 1. The simulated diffraction patterns from the solved crystal structures were compared with the experimental diffraction patterns of these materials, which suggests that representative solutions were obtained (see the SI) and that these materials exist as single phases. Representations of the asymmetric unit, crystal packing along with the a, b, and c axes, and Oak Ridge Thermal Ellipsoid Plot (ORTEP) for each BPBPA-based BPCP are provided in the SI. Each crystal structure presents a unique extended 3D framework in which the organic ligand serves as a bridge interconnecting the metal centers. Interestingly, all crystal phases present channels, BPBPA-Ca (11 × 12 Å), BPBPA-Zn (10 × 13 Å), and BPBPA-Mg (8 × 11 Å), that

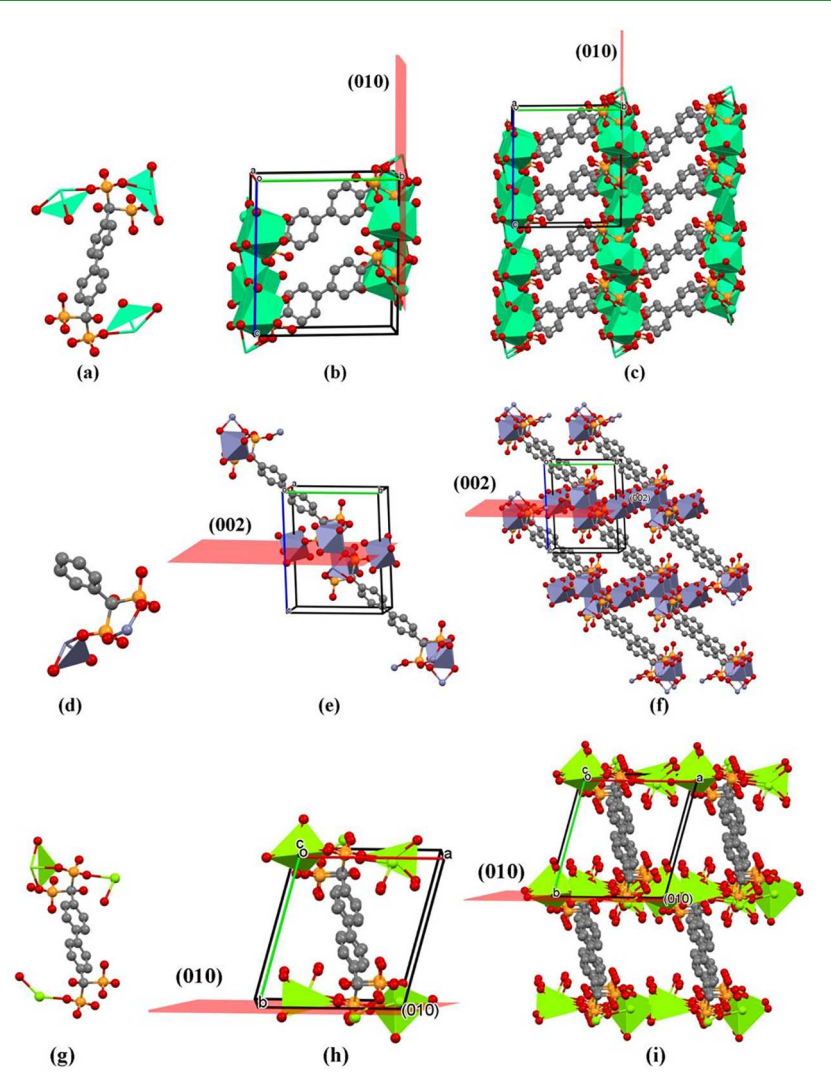


**Figure 4.** Asymmetric units (a, d, and g), unit cells (b, e, and h), and  $2 \times 2 \times 2$  packings (c, f, and i) along the c axis of BPBPA-Ca (top), BPBPA-Zn (middle), and BPBPA-Mg (bottom). Hydrogen atoms in the ligand, lattice, and coordinated water molecules were omitted for clarity.

enable the use of these 3D frameworks as possible DDSs. The crystallographic files related to BPBPA-Ca (2239635), BPBPA-Zn (2239636), and BPBPA-Mg (2239637) were deposited to the Cambridge Crystallographic Data Center (CCDC).

BPBPA-Ca.  $[Ca_3(C_{14}H_8O_{14}P_4)(6H_2O)]\cdot 7H_2O$  represents the empirical formula of BPBPA-Ca, a material that crystallizes in the triclinic P1 space group. It was observed that the asymmetric unit of BPBPA-Ca contains one molecule of the BP ligand coordinated with three distinct Ca<sup>2+</sup> metal centers (Figure 4a). A total of six coordinated water molecules were found in BPBPA-Ca, where two water molecules complete the coordination sphere in each metal center (Ca1, Ca2, and Ca3) per asymmetric unit. Close examination of the crystal packing (Figure 4b,c) of this material reveals that the metal centers (Ca<sup>2+</sup>) are interconnected by BP-bridged ligands, which leads to a continuous 3D framework parallel to the (010) hkl plane. The Ca<sup>2+</sup> ions display distorted-bicapped trigonal-prismatic (Ca1 and Ca3) and capped trigonal-prismatic (Ca2) geometries, respectively. The -Ca1-O presents polar bond angles ( $\theta$ ) ranging between 45.32 and 58.08° and a bond angle ( $\alpha$ ) between the capped ligands of 126.14°, while O-Ca3-O displays  $\theta$  angles between 44.82 and 54.34° and an  $\alpha$  angle of 112.90°. The bond angles in the coordination spheres of Ca1 and Ca3 are distorted by  $0.18-13.08^{\circ}$  ( $\theta$ ) and  $6.14-7.1^{\circ}$  ( $\alpha$ )

compared with a regular bicapped trigonal-prismatic geometry, where  $\theta = 45^{\circ}$  and  $\alpha = 120^{\circ}$ . The O-Ca2-O exhibit bond angles varying from 68.91 to 82.88°; these angles are distorted by 5.88-8.09° from a regular capped trigonal-prismatic molecular geometry, where the predicted bond angle is ~77° 33 Furthermore, the Ca1-O, Ca2-O, and Ca3-O bond distances are in the ranges 2.311-2.767, 2.313-2.559, and 2.402–2.534 Å, respectively. The Ca–O bond distances in BPBPA-Ca are similar to those found in other BP-based BPCCs obtained using commercial BPs such as etidronic acid (HEDP), ALEN, RISE, or ZOLE (average =  $2.4 \pm 0.1 \text{ Å}$ ) and found in the CCDC. 21-23,34-37 In addition, the crystal structure of BPBPA-Ca displays channels (11 Å × 12 Å) formed by adjacent BP-bridged ligands that provide sufficient void space for the integration of seven disordered uncoordinated water molecules (see the SI).

*BPBPA-Zn*. The empirical formula of BPBPA-Zn was determined as  $[Zn_3(C_{14}H_8O_{14}P_4)(4H_2O)]\cdot 4H_2O$ . BPBPA-Zn crystallizes in the P1 space group and contains a half ligand molecule coordinated with two unique  $Zn^{2+}$  metal ions in the asymmetric unit (Figure 4d). Two coordinated water molecules can be found in the coordination sphere of the Zn2 metal center. A close assessment of the crystal packing (Figure 4e,f) of BPBPA-Zn shows that the  $Zn^{2+}$  metal centers

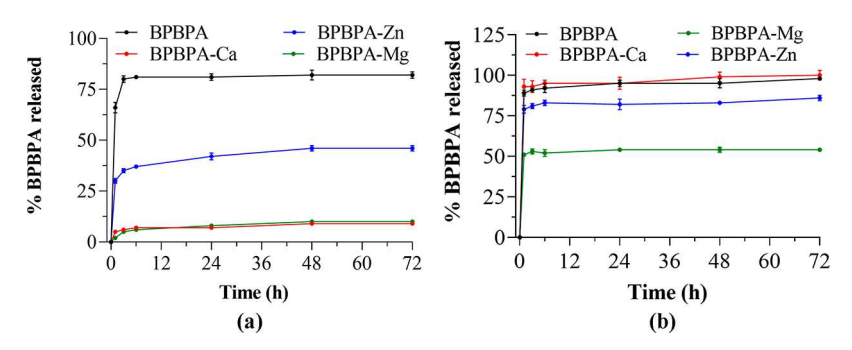


Figure 5. Dissolution curve for BPBPA (black), BPBPA-Ca (red), BPBPA-Zn (blue), and BPBPA-Mg (green) in (a) PBS (pH = 7.4) and (b) FaSSGF (pH = 1.6) at 37 °C. Each experiment was performed in duplicate. If error bars are not observed, this indicates a small %CV (<5%).

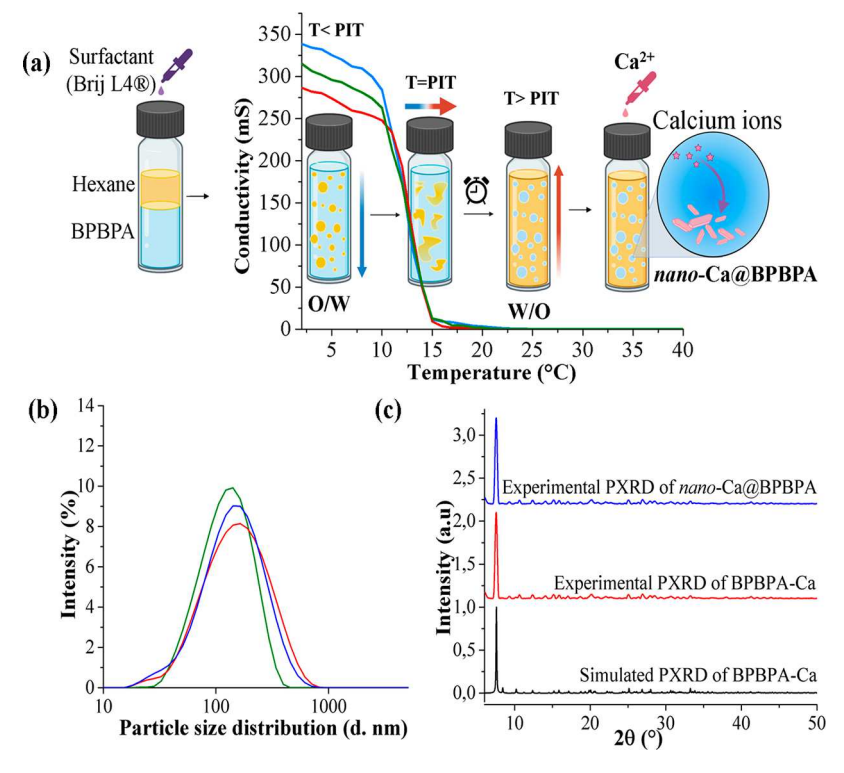


Figure 6. (a) Schematic diagram of the PIT-nanoemulsion synthesis of nano-Ca@BPBPA. The PIT was determined to occur at about ~12 °C. <sup>10</sup> (b) DLS spectra showing the particle size distribution (168  $\pm$  9 d. nm; %CV = 5%) for three syntheses of nano-Ca@BPBPA. (c) Experimental diffraction patterns of BPBPA (black), BPBPA-Ca (red), and nano-Ca@BPBPA (blue).

are interconnected through BP-bridged ligands, producing a 3D framework parallel to the (002) hkl plane. The Zn<sup>2+</sup> metal centers (Zn1 and Zn2) exhibit a distorted octahedral geometry. This geometry is usually found in Zn2+ ions with 6-fold coordination numbers. 38 The O-Zn1-O and O-Zn2-O bond angles are in the ranges of 74.18-108.59° and 84.10-95.90°, respectively. The bond angles in the coordination spheres of the Zn1 and Zn2 metal centers are distorted by 5.9-18.59° from a regular octahedral molecular geometry, where the predicted bond angle is 90°. 38 The Zn1-O and Zn2-O bond distances are in the ranges of 1.989-2.365 and 2.022-2.167 Å, respectively. The Zn1-O and Zn2-O bond distances found in BPBPA-Zn are comparable to those observed in other BP-based BPCCs synthesized using commercial BPs (HEDP, ALEN, RISE, or ZOLE) coordinated with a  $\rm Zn^{2+}$  metal center (average = 2.1  $\pm$  0.1 Å) and found in the CCDC. 21-23,39,40 Additionally, neighboring BPs-bridge ligands generate channels ( $10 \times 13 \text{ Å}$ ) in this framework that

facilitate the incorporation of four uncoordinated water molecules which present disorder (see the SI).

BPBPA-Mg. This material shows an empirical formula of  $[Mg_3(C_{14}H_8O_{14}P_4)(6H_2O)]\cdot 7H_2O$  and crystallizes in the triclinic  $\overline{P1}$  space group. It was observed that the asymmetric unit of BPBPA-Mg (Figure 4g) contains one ligand coordinated with three distinctive Mg2+ metal centers. One coordinated water molecule completes the coordination of the Mg2 and Mg3 metal centers, respectively. The interconnection between the BP-bridged ligands and the Mg<sup>2+</sup> metal ions (Figure 4h) leads to a continuous 3D framework parallel to the (100) hkl plane (Figure 4i). The Mg<sup>2+</sup> metal centers depict distorted T-shaped (Mg1), seesaw (Mg2), and bent (Mg3) molecular geometries. These molecular geometries have been observed previously in Mg<sup>2+</sup> ions with 2-, 3-, and 4-fold coordination numbers. The O-Mg1-O shows bond angles of 78.83 and 134.54° in a distorted T-shaped geometry, where the predicted bond angles are  $<90^{\circ}$  and  $>120^{\circ}$ . The O-Mg2-O bond angle ranges between 80.56° and 121.89°,

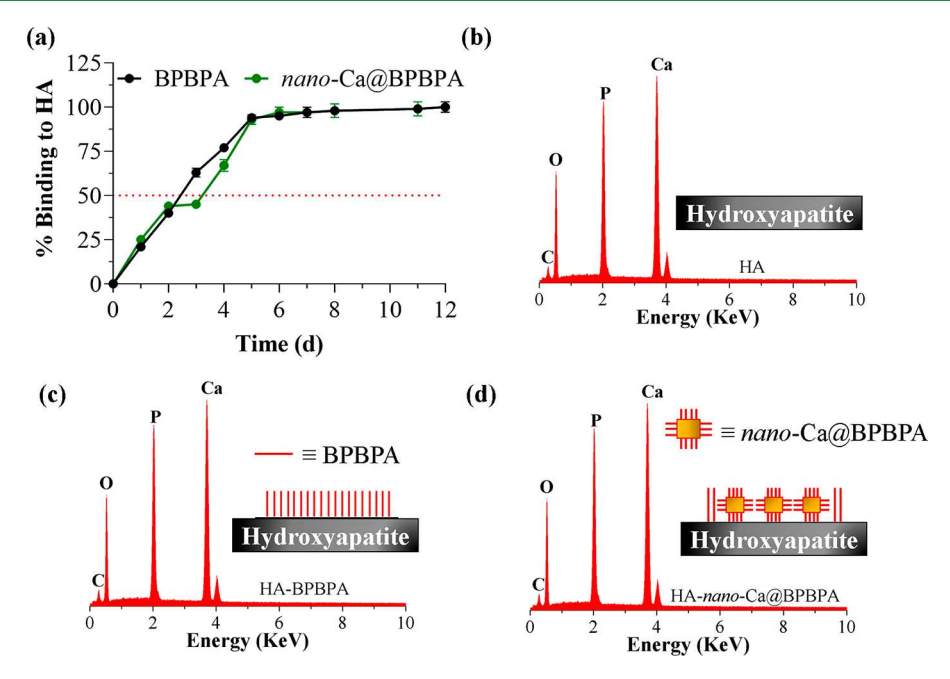


Figure 7. (a) Binding curves in a simulated physiological buffer (PBS, pH = 7.4) for BPBPA and nano-Ca@BPBPA to HA at 37 °C. If error bars are not observed, this indicates a small coefficient of variation (%CV < 5%). Elemental analysis for (b) HA, (c) HA-BPBPA, and (d) HA-nano-Ca@BPBPA. These experiments were performed at 3000× magnification. The inset schematic diagrams in parts b—d show the proposed binding of BBPA and nano-Ca@BBPA to HA.

compared with a regular seesaw geometry, where the predicted bond angles are <90° and <120° between adjacent atoms. For the Mg3 metal centers, the O–Mg3–O bond angle is 76.19° in a distorted bent geometry (<120°). The Mg–O bond distances vary from 2.342 to 2.406 Å, from 2.337 to 2.395 Å, and from 2.400 to 2.416 Å for Mg1–O, Mg2–O, and Mg3–O, respectively. The Mg–O bond distances in BPBPA-Mg are comparable to those observed in the crystal structures of other BP-based BPCCs (average = 2.1  $\pm$  0.1 Å),  $^{21-23,44,45}$  where commercial BPs such as ALEN, ZOLE, or RISE are coordinated Mg<sup>2+</sup> ions. Furthermore, it was observed that adjacent BP-bridged ligands form channels (8 Å  $\times$  11 Å), presenting void spaces that, in this case, incorporate seven disordered lattice water molecules (see the SI).

The dissolution curves were obtained in simulated physiological buffers (PBS, pH = 7.40; FaSSGF, pH = 1.60) by measuring the absorbance of the supernatant to quantify the amount of BPBPA released over time in PBS ( $\lambda_{max} = 275 \text{ nm}$ ) and FaSSGF ( $\lambda_{max}$  = 266 nm) at 37 °C. The results show that the free ligand, BPBPA, dissolves readily (82% in PBS and 98% in FaSSGF within 72 h) in both buffers due to its aqueous solubility (20 mg/mL in nanopure water at 25 °C and pH = 7.0). The results also revealed that BPBPA-based BPCPs release 9-50% of BPBPA under neutral conditions; specifically, BPBPA-Ca, BPBPA-Zn, and BPBPA-Mg resulted in 9, 46, and 10% release of BPBPA (Figure 5a) after 72 h. Furthermore, it was found that these coordination polymers release 50-100% of BPBPA under acidic conditions, resulting in 100, 86, and 54% release of BPBPA from BPBPA-Ca, BPBPA-Zn, and BPBPA-Mg, respectively (Figure 5b) within a 72 h period. In particular, these results show that the structure of BPBPA-Ca is preserved in PBS (~10% release of BPBPA), while in FaSSGF, the structure collapses (~100% release of BPBPA). These findings suggest that a drug-loaded version of BPBPA-Ca might be able to degrade, elicited by the acidic pH

of neoplastic cells and their metabolism, potentially releasing its cargo at the target site, the bone.  $^{46}$ 

The particle size of BPBPA-Ca was reduced using the PIT-nanoemulsion method. <sup>21–24</sup> BPBPA-Ca (11 Å × 12 Å) was selected because this material displayed the highest synthesis yield, largest channels, and more drastic pH degradation, potentially enabling maximum delivery of encapsulated drugs to the target site. The PIT temperature was determined for an emulsion constituted of an aqueous solution of BPBPA with heptane (oil phase) and Brij L4 (surfactant). The PIT was determined through conductivity ( $\sigma$ ) measurements, while the emulsion was heated from 2 to 40 °C, as described in the SI. A drastic change in the emulsion conductivity is observed due to the phase inversion from an oil-in-water (O/W) microemulsion ( $\sigma$  = 313  $\mu$ S) to a water-in-oil (W/O) nanoemulsion ( $\sigma$  = 0.061  $\mu$ S). The PIT for this system starts at 7 °C and ends at 17 °C, resulting in an average PIT temperature of ~12 °C (see the SI).

Upon reaching the PIT, this method forms a W/O nanoemulsion, where aqueous nanospheres contain the free ligand. Once added, the metal salt solution promotes the formation of *nano*-Ca@BPBPA (Figure 6a) within this limited volume, which in terms limits the size of the resulting crystalline particles. The particle size distribution and polydispersity index (PDI) ranged between 166 and 180 d. nm and between 0.493 and 0.538, respectively, in three separate syntheses. These results demonstrate that this material possessed a monodisperse particle size distribution of <500 nm, representing an adequate particle size to penetrate a cell membrane <sup>47,48</sup> (Figure 6b). Additionally, the PXRD patterns of an agglomerate of *nano*-Ca@BPBPA (Figure 6c) confirmed that the material synthesized by the PIT-nanoemulsion method is isostructural to BPBPA-Ca.

The propensity of nano-Ca@BPBPA to agglomerate over time in 10% FBS/PBS was assessed via DLS measurements. The results reveal that nano-Ca@BPBPA maintains a

Table 2. EDS Elemental Analysis of BPBPA, nano-Ca@BPBPA, HA, a 1:1 Physical Mixture of HA/nano-Ca@BPBPA, HA-BPBPA, and HA-nano-Ca@BPBPA<sup>a</sup>

element (wt %)	BPBPA <sup>c</sup>	nano-Ca@ BPBPA	HA <sup>b</sup>	physical mixture (1:1) HA/nano-Ca@BPBPA	НА-ВРВРА	HA-nano-Ca@ BPBPA
phosphorus	$19.71 \pm 0.09$	$18.03 \pm 0.04$	$19.70 \pm 0.03$	$16.31 \pm 0.03$	$19.65 \pm 0.04$	$19.01 \pm 0.05$
oxygen	$37.25 \pm 0.3$	$28.51 \pm 0.2$	$30.57 \pm 0.1$	$22.58 \pm 0.1$	$33.71 \pm 0.2$	$34.64 \pm 0.2$
calcium		$17.38 \pm 0.08$	$41.89 \pm 0.06$	$26.34 \pm 0.05$	$33.88 \pm 0.07$	$34.27 \pm 0.06$
carbon	$43.04 \pm 0.07$	$36.08 \pm 0.03$	$7.84 \pm 0.03$	$34.78 \pm 0.06$	$12.76 \pm 0.04$	$12.08 \pm 0.05$

"The EDS analysis was performed at a 3000× magnification for all samples.  ${}^{b}HA = [Ca_{5}(OH)(PO_{4})_{3}]$ . "BPBPA =  $[C_{14}H_{18}O_{14}P_{4}]$ . "nano-Ca@ BPBPA =  $[Ca_{3}(C_{14}H_{8}O_{14}P_{4})(6H_{2}O)]$ ."7H<sub>2</sub>O.

Table 3. Elemental Analysis of LET (Control), BPBPA-Ca (Control), nano-Ca@BPBPA (Control), Drug-Loaded BPBPA-Ca (Experimental), and Drug-Loaded nano-Ca@BPBPA (Experimental) after the Drug Loading Experiment by SEM-EDS<sup>a</sup>

element (wt %)	LET <sup>b</sup>	BPBPA-Ca <sup>c</sup>	nano-Ca@BPBPA <sup>d</sup>	drug-loaded BPBPA-Ca	drug-loaded nano-Ca@BPBPA
phosphorus		$17.40 \pm 0.01$	$17.01 \pm 0.05$	$13.69 \pm 0.02$	$14.34 \pm 0.08$
oxygen		$27.46 \pm 0.1$	$27.93 \pm 0.3$	$25.30 \pm 0.1$	$25.53 \pm 0.1$
calcium		$16.65 \pm 0.01$	$16.36 \pm 0.05$	$13.02 \pm 0.01$	$13.78 \pm 0.02$
carbon	$87.20 \pm 0.04$	$38.49 \pm 0.09$	$38.70 \pm 0.2$	$47.38 \pm 0.08$	$45.93 \pm 0.08$
nitrogen	$12.80 \pm 0.2$			$0.61 \pm 0.2$	$0.42 \pm 0.3$

<sup>a</sup>The analysis was collected at 3000× magnification for all of the samples. <sup>b</sup>LET =  $[C_{17}H_{11}N_5]$ . <sup>c</sup>BPBPA = Ca $[C_{14}H_{18}O_{14}P_4]$ . <sup>d</sup>nano-Ca@BPBPA =  $[Ca_3(C_{14}H_8O_{14}P_4)(6H_2O)]$ ·7H<sub>2</sub>O.

homogeneous particle size distribution in 10% FBS/PBS after 0 h (170 d. nm), 24 h (182 d. nm), and 48 h (181 d. nm). Furthermore, the resulting PDI values after 0 h (0.488), 24 h (0.501), and 48 h (0.479) confirm the monodispersity of *nano-Ca@BPBPA* at the three time points (see the SI). These results demonstrate that *nano-Ca@BPBPA* does not agglomerate significantly over time in 10% FBS/PBS; larger aggregates were not formed, a characteristic that might promote its possible use for biomedical applications.

Binding Assays for nano-Ca@BPBPA. The binding of nano-Ca@BPBPA to HA, to the main constituent of bone, 49,50 was assessed in a simulated physiological buffer (PBS, pH = 7.4, and 37 °C), exposing this material to nano-Ca@BPBPA (5 mL, 0.5 mg/mL BPBPA, experimental) for 0-12 days. In addition, BPBPA (5 mL, 0.5 mg/mL BPBPA) and HA (20 mg) were used as controls (see the SI). The affinity to HA was determined by quantifying the decrease in the concentration of BPBPA and nano-Ca@BPBPA in the supernatant using absorbance measurements ( $\lambda_{\text{max}} = 275 \text{ nm}$ ). The binding curves for BPBPA and nano-Ca@BPBPA are shown in Figure 7a. It was found that BPBPA presents >70% (3 days) binding to HA, reaching >90% after 4 days in PBS. Additionally, nano-Ca@BPBPA demonstrates a similar binding to HA. These results indicate that nano-Ca@BPBPA possesses higher affinity to the bone than those reported for commercial (1.7 and 1.4 times higher than those of ZOLE and RISE, respectively), 22,23 and extended BPs (1.9 times higher than that of BBPA)<sup>24</sup> at 24 h. In PBS, most of nano-Ca@BPBPA remains coordinated (~10% release of BPBPA in 72 h), and its structure is intact; therefore, it is suggested that the uncoordinated BPs on the nano-Ca@BPBPA surface are able to bind to HA (see the SI).

The elemental compositions of BPBPA (control), nano-Ca@BPBPA (control), HA (control, Figure 7b), HA-BPBPA (experimental), and HA-nano-Ca@BPBPA (experimental) were contrasted using the weight percentage (wt %) obtained by EDS to confirm the binding to HA (Table 2 and the SI). The results reveal that the phosphorus signals found in HA-BPBPA (19.65 wt %, Figure 7c) and HA-nano-Ca@BPBPA (19.01 wt %, Figure 7d) were comparable to that detected in

HA (19.70 wt %). This was expected due to the similar composition of this element in BPBPA (19.71 wt %; 4 phosphorus atoms per formula unit) and nano-Ca@BPBPA (18.03 wt %; 4 phosphorus atoms per asymmetric unit). An increase in the relative composition of the oxygen signal was observed when contrasting HA-BPBPA (33.71 wt %) and HAnano-Ca@BPBPA (34.64 wt %) to HA (30.57 wt %). This result supports the presence of BPBPA (37.25 wt %; 14 oxygen atoms per formula unit) and nano-Ca@BPBPA (28.51 wt %; 27 oxygen atoms per asymmetric unit) on the surface of HA. The difference between the free versus bound materials might be due to the presence of a monolayer (BPBPA) or the deposition of particles (nano-Ca@BPBPA) on the HA surface. Furthermore, the results demonstrate a decrease in the relative composition of the calcium signal in HA-BPBPA (33.88 wt %) and HA-nano-Ca@BPBPA (34.27 wt %) when contrasted with HA (41.89 wt %). This result was expected due to the proposed binding of BPBPA (0 wt %; 0 calcium atoms per formula unit) and nano-Ca@BPBPA (17.38 wt %; 3 calcium atoms per asymmetric unit) on the HA surface (41.89 wt %; 5 calcium atoms per formula unit) that might shield the detection of calcium ions. The conductive tape used for the SEM-EDS analysis led to a small amount of carbon (7.84 wt %) detected in the EDS spectra of HA. The carbon signal was found in HA-BPBPA (12.76 wt %) and HA-nano-Ca@BPBPA (12.08 wt %). The signal for the latter two increases as a result of the molecular structure of BPBPA (43.04 wt % carbon) and nano-Ca@BPBPA (36.08 wt % carbon), which contains 14 carbon atoms per formula or asymmetric unit, respectively. A 1:1 physical mixture of ground HA/nano-Ca@BPBPA was also used as the control group (see the SI), and the differences observed in the elemental composition of HA/nano-Ca@ BPBPA (i.e., 26.34 wt % calcium and 34.78 wt % carbon) confirm the binding of BPBPA and nano-Ca@BPBPA (~34 wt % calcium and ~12 wt % carbon for HA-BPBPA and HA-nano-Ca@BPBPA) to the surface of HA.

**Loading and Release of LET into BPBPA-Ca and** *nano-*Ca@BPBPA. LET, an antineoplastic drug prescribed to treat breast cancer therapy<sup>51,52</sup> and combined with BPs to treat

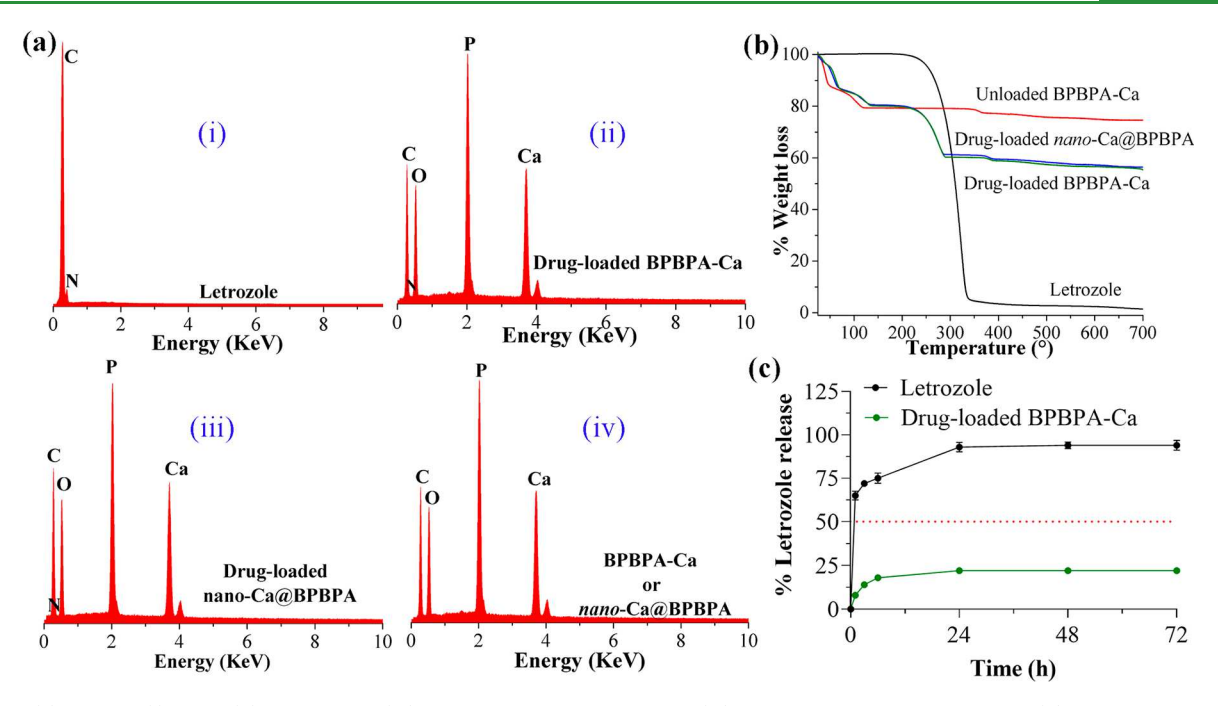


Figure 8. (a) EDS of (i) LET, (ii) BPBPA-Ca, (iii) drug-loaded BPBPA-Ca, and (iv) drug-loaded nano-Ca@BPBPA. (b) TGA thermographs of LET (black) and BPBPA-Ca (green) compared with the TGA thermographs of drug-loaded BPBPA-Ca (blue) and nano-Ca@BPBPA (red). (c) Percent release curve of LET (black, control) and drug-loaded BPBPA-Ca (green, experimental) in FaSSGF (pH = 1.60) at 37 °C. This experiment was performed in duplicate. If error bars are not observed, this indicates a small %CV (<5%).

ER-positive breast-cancer-induced OM, <sup>53–55</sup> was encapsulated into the channels of BPBPA-Ca and *nano*-Ca@BPBPA. The loading of LET into BPBPA-Ca was performed in ethanol as the solvent; this framework was exposed to LET for 24 h at 50 °C, leading to drug-loaded BPBPA-Ca (see the SI). In the case of *nano*-Ca@BPBPA, the PIT-nanoemulsion method was coupled to the loading of LET. After the PIT synthesis of *nano*-Ca@BPBPA, a LET solution was added, and the mixture was left under constant stirring for 1 h, to yield the drug-loaded *nano*-Ca@BPBPA (see the SI). Furthermore, LET, empty, and drug-loaded BPBPA-Ca and empty and drug-loaded *nano*-Ca@BPBPA were characterized by EDS and/or PXRD (see the SI).

The loading of LET was confirmed by contrasting the weight percentage (wt %) of all elements detected by EDS with the empty and drug-loaded versions of BPBPA-Ca and nano-Ca@BPBPA (Table 3). The elemental analysis of LET was used as a control [Figure 8a(i)]. The elements phosphorus, oxygen, and calcium were not detected in LET due to the absence of these elements in the chemical structure of this compound. Similar relative concentrations of phosphorus (14-17 wt %), oxygen (25-28 wt %), and calcium (13-17 wt %) were observed for drug-loaded BPBPA-Ca [Figure 8a(ii)] and drug-loaded nano-Ca@BPBPA [Figure 8a(iii)] compared with BPBPA-Ca and nano-Ca@BPBPA [Figure 8a(iv)]. This result is due to the absence of these elements in the molecular structure of LET (0 atoms per formula unit). Furthermore, an increase in the relative concentration of carbon was observed for the drug-loaded BPBPA-Ca (47.38 wt %) and nano-Ca@BPBPA (45.93 wt %) contrasted with BPBPA-Ca (38.49 wt %) and nano-Ca@ BPBPA (38.72 wt %). This result might be attributed to the presence of carbon in the molecular structure of LET (17 carbons per formula unit). Moreover, a small amount of nitrogen was detected in the drug-loaded BPBPA-Ca (0.61 wt %) and nano-Ca@BPBPA (0.42 wt %). Nitrogen was not

detected in BPBPA-Ca and nano-Ca@BPBPA due to the absence of this element in these materials. The relative concentration of nitrogen in the drug-loaded materials decreases in contrast with LET (12.80 wt %), indicating that the encapsulation of this drug into the BPCPs might have shielded the detection of this characteristic element in LET.

Furthermore, the release of LET from the drug-loaded BPBPA-Ca was investigated in FaSSGF (pH = 1.60) at 37 °C by measuring the increase in the LET concentration over time  $(\lambda_{\text{max}} = 238 \text{ nm})$  in this medium (see the SI). The release of LET in FaSSGF from the drug-loaded nano-Ca@BBPA was not conducted due to the difficulty in obtaining an adequate amount of this material to perform this experiment. The drugloaded BPBPA-Ca reaches a maximum release of LET (22 wt %) with 24 h. This result is in agreement with the amount (%) of LET encapsulated into BPBPA-Ca and nano-Ca@BPBPA determined by TGA: 22-24 wt % (TGA, Figure 8b) versus 22 wt % (FaSSGF, Figure 8c). These results parallel those reported for BPDC-based CPs [i.e., UiO-67-(NH<sub>2</sub>)<sub>2</sub> (11 Å), <sup>18</sup> BPDC-Zr (~12 Å), 12 bio-MOF-1 (7 and 10 Å), 20], where antineoplastic drugs, such as pemetrexed and Ru-90, and other pharmaceutical compounds, such as calcein and  $\alpha$ -cyano-4hydroxycinnamic acid, were loaded and then released in PBS (see the SI).

**Cell Viability Assays for** *nano***-Ca@BPBPA.** The cytotoxicity of BPBPA, LET, *nano*-Ca@BPBPA, and drugloaded *nano*-Ca@BPBPA was investigated by employing the human breast cancer, MCF-7 and MDA-MB-231, and human osteoblast, hFOB 1.19, cell lines. The human MCF-7 cell line represents an ER-positive breast cancer model expressing estrogen, progesterone, and glucocorticoid receptors. LET is a type II aromatase inhibitor that avoids the transformation of androgens to estrogens by the aromatase enzyme; this action is crucial in treating ER-positive breast cancer types (represented in this work by MCF-7 cells). S6-58 The human MDA-MB-231

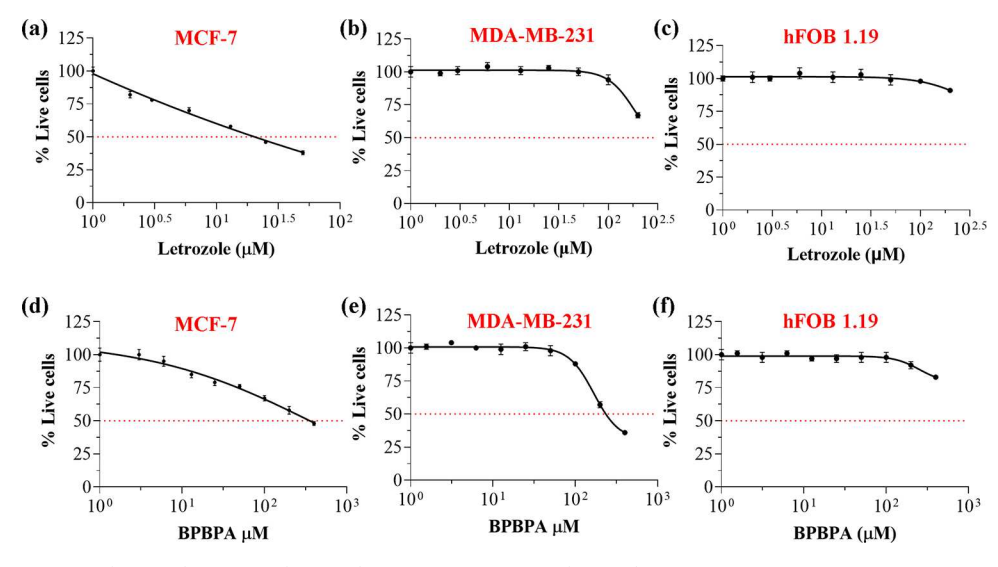


Figure 9. IC<sub>50</sub> curves for the (a and d) MCF-7, (b and e) MDA-MB-231, and (c and f) hFOB 1.19 cell lines treated with LET (0–200  $\mu$ M, top) and BPBPA (0–400  $\mu$ M, bottom) after 72 h of treatment. The experiments were performed in triplicate. If error bars are not observed, this indicates a small %CV (<5%).

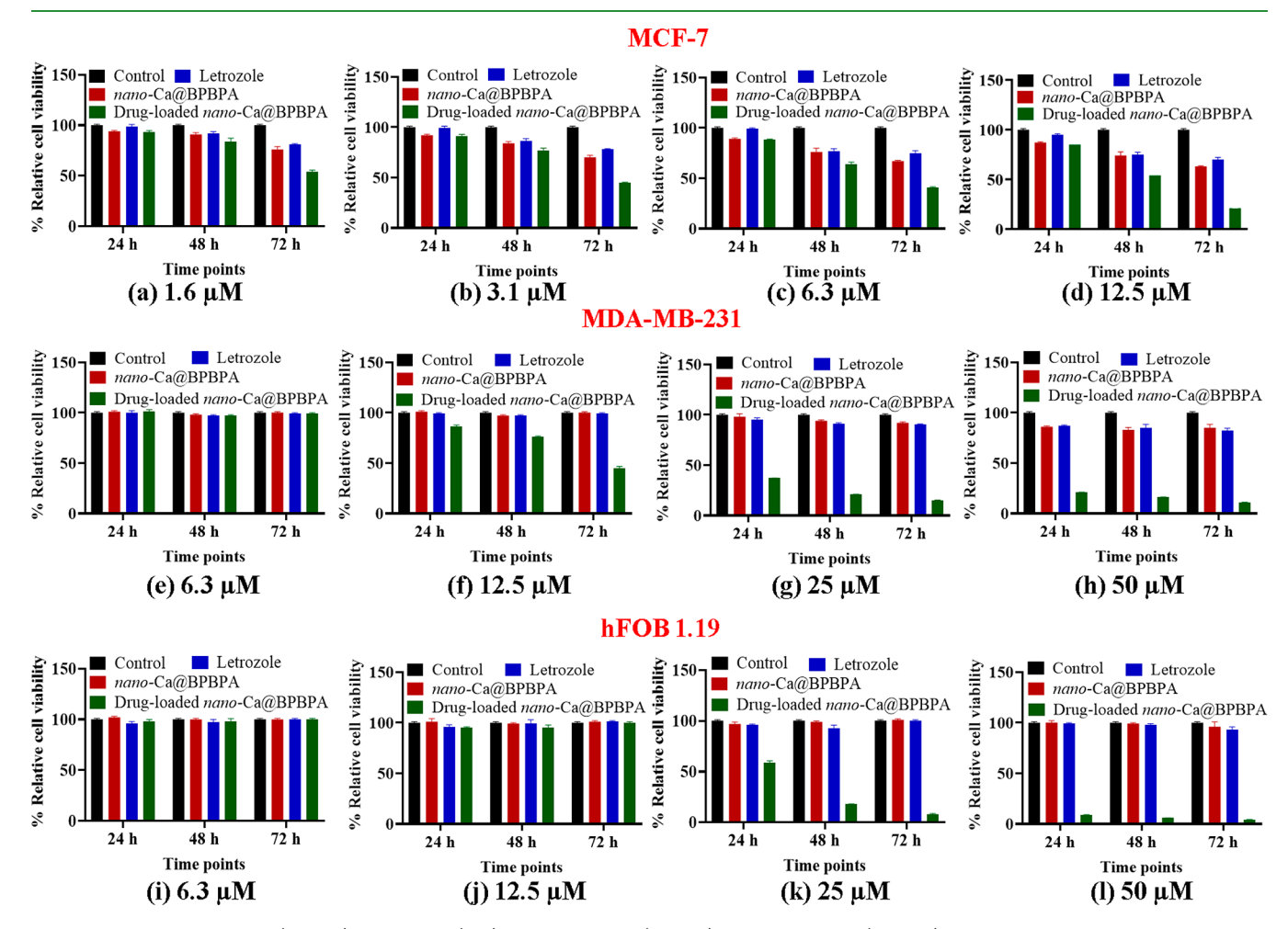


Figure 10. Relative cell lives (%RCV) for MCF-7 (top), MDA-MB-231 (middle), and hFOB 1.19 (bottom) cells treated with DMEM or DMEM/F12 (control, black), *nano*-Ca@BPBPA (experimental, red), LET (experimental, blue), and drug-loaded *nano*-Ca@BPBPA (experimental, green) in concentrations of (a) 1.6, (b) 3.1, (c, e, and i) 6.3, (d, f, and j) 12.5, (g and k) 25, and (h and l) 50 μM after 24, 48, and 72 h of treatment.

cell line corresponds to a model of TNBC (negative for ER, PR, and HER2 receptors). <sup>59,60</sup> In the case of TNBC, represented here by the MDA-MB-231 cell line, the

cytotoxicity of LET is expected to be lower because this cell line does not depend on estrogen signaling. Both selected cancer cell lines represent two distinct breast cancer subtypes, ER-positive and TNBC, with the ability to metastasize to the bone. 1,5-7,59,60 The human fetal hFOB 1.19 cells represent a homogeneous osteoblast-like (noncancerous) model commonly employed to assess osteoblast differentiation. 61 In this work, the noncancerous hFOB 1.19 cells were employed to represent the healthy bone microenvironment. The cytotoxicity of these materials was evaluated by determining IC<sub>50</sub> and %RCV. The results show a decrease in the cell viability of MCF-7 cells treated with LET, with IC<sub>50</sub> of about 20  $\pm$  3  $\mu$ M after 72 h of treatment (Figure 9a and the SI). This IC<sub>50</sub> value is consistent with reports where similar seeding and treatment conditions were employed (IC<sub>50</sub> =  $\sim$ 15–20  $\mu$ M).<sup>62,63</sup> No significant cytotoxicity effects were observed for MDA-MB-231 and hFOB 1.19 cell lines treated with LET (Figure 9b,c;  $IC_{50}$  > 200 µM after 72 h). Similar results were found for MCF-7 (Figure 9d), MDA-MB-231 (Figure 9e), and hFOB 1.19 (Figure 9f) cells treated with BPBPA (IC<sub>50</sub> > 200  $\mu$ M after 72 h), with calculated IC<sub>50</sub> =  $364 \pm 3 \mu M$  for MCF-7 and  $229 \pm 5$  $\mu$ M for MDA-MB-231 cells treated with BPBPA at 72 h. IC<sub>50</sub> curves for the MCF-7, MDA-MB-231, and hFOB 1.19 cell lines treated with LET and BPBPA at 24, 48, and 72 h are shown in the SI.

The MCF-7 cells were treated with LET and empty and drug-loaded nano-Ca@BPBPA in the concentration range of 1.6-12.5  $\mu$ M (Figure 10a-d). The results at 1.6  $\mu$ M demonstrate that LET, nano-Ca@BPBPA, and drug-loaded nano-Ca@BPBPA did not display significant cytotoxicity against the MCF-7 cells after 24 h (%RCV > 93%) and 48 h (%RCV > 84%) of treatment. A higher cytotoxicity effect was observed for the drug-loaded nano-Ca@BPBPA (%RCV = 54  $\pm$  3%) in contrast with nano-Ca@BPBPA (%RCV = 76  $\pm$  4%) and LET (%RCV = 81%) after 72 h (Figure 10a). Furthermore, it was noticed that the cell viability was >90% for the MCF-7 cells treated at a concentration of 3.1  $\mu$ M with LET (%RCV = 99  $\pm$  2%), nano-Ca@BPBPA (%RCV = 92  $\pm$ 1%), and drug-loaded nano-Ca@BPBPA (%RCV = 91  $\pm$  2%) after 24 h. A slight decrease in the cell viability was detected after 48 h for LET (%RCV =  $86 \pm 3\%$ ), nano-Ca@BPBPA (% RCV =  $84 \pm 2\%$ ), and drug-loaded nano-Ca@BPBPA (%RCV = 77  $\pm$  3%). At 72 h, it was observed that drug-loaded nano-Ca@BPBPA (%RCV =  $45 \pm 2$ %) presented a higher decrease in the cell viability than LET (%RCV =  $78 \pm 1\%$ ) and nano-Ca@BPBPA (%RCV =  $70 \pm 3\%$ ; Figure 10b). Similar results were found at a concentration of 6.3  $\mu$ M; the cell viability remained >88% after 24 h for LET (%RCV = 99  $\pm$  1%), nano-Ca@BPBPA (%RCV =  $89 \pm 1$ %), and drug-loaded nano-Ca@ BPBPA (%RCV =  $88 \pm 1$ %). The results show a higher decrease in the cell viability after 72 h for drug-loaded nano-Ca@BPBPA (%RCV =  $41 \pm 1$ %) compared with LET (%RCV = 75  $\pm$  3%) and nano-Ca@BPBPA (%RCV = 67  $\pm$  1%; Figure 10c). At a concentration of 12.5  $\mu$ M, a higher decrease in the cell viability was observed for MCF-7 cells treated with drugloaded nano-Ca@BPBPA (%RCV =  $21 \pm 1\%$ ) compared with LET (%RCV =  $70 \pm 3$ %) and nano-Ca@BPBPA (%RCV = 63± 1%) after 72 h (Figure 10d). These results demonstrate higher cytotoxicity effects by drug-loaded nano-Ca@BPBPA against MCF-7 cancerous cells than LET and nano-Ca@ BPBPA at concentrations of 1.6–12.5  $\mu$ M, values below IC<sub>50</sub>  $(20 \pm 3 \mu M \text{ at } 72 \text{ h})$  when cells were treated with LET.

Additionally, MDA-MB-231 cells were treated with LET, empty, and drug-loaded nano-Ca@BPBPA at a higher concentration range of 6.3–50  $\mu$ M for 24, 48, and 72 h. The %RCV results demonstrate that nano-Ca@BPBPA and LET

did not lead to a significant decrease in the cell viability in MDA-MB-231 cells (Figure 10e-h) after treatment (%RCV > 92%) at the three time points. At a concentration of 6.3  $\mu$ M, drug-loaded nano-Ca@BPBPA presented cytotoxicity similar to that of LET, showing %RCV > 97% (Figure 10e). At 12.5 μM, drug-loaded nano-Ca@BPBPA presents a decrease in the cell viability after 24 h (%RCV =  $86 \pm 1\%$ ), 48 h (%RCV = 76 $\pm$  1%), and 72 h (%RCV = 45  $\pm$  4%) of treatment, contrasted with LET (Figure 10f). Higher cytotoxicity effects were found for drug-loaded nano-Ca@BPBPA at a concentration of 25 μM after 24 h (%RCV =  $37 \pm 1$ %), 48 h (%RCV =  $21 \pm 1$ %), and 72 h (%RCV = 8 ± 1%; Figure 10g). At 50  $\mu$ M, a slight decrease in the cell viability was observed for LET and nano-Ca@BPBPA after 24 h (%RCV  $\sim$  86%), 48 h (%RCV  $\sim$  83%), and 72 h (%RCV ~ 82%) of treatment. A higher cytotoxicity effect was found for drug-loaded nano-Ca@BPBPA after 24 h  $(\%RCV = 21 \pm 1\%)$ , 48 h  $(\%RCV = 16 \pm 2\%)$ , and 72 h (%RCV =  $11 \pm 1\%$ ; Figure 10h). These results demonstrate that drug-loaded nano-Ca@BPBPA presented higher cytotoxicity to the selected cancerous model (MDA-MB-231) than LET and nano-Ca@BPBPA at the concentrations range of 6.3-50 μM, resulting in values lower than IC<sub>50</sub> of >200  $\mu$ M after 72 h when MDA-MB-231 cells were treated with LET. Furthermore, it was observed that the cytotoxicity effects were lower for MDA-MB-231 cells compared with MCF-7 cells, which was expected due to the fact that MDA-MB-231 is a TNBC cell line.

These cell viability results suggest that drug-loaded nano-Ca@BPBPA might improve the drug-delivery efficiency in MCF-7 and MDA-MB-231. In MCF-7 cells, LET can lead to cell apoptosis by inhibiting the aromatase enzyme, while in MDA-MB-231, LET might lead to diverse gene expression levels, affecting cell pro-apoptotic (stress or death) or antiapoptotic (mitogenic or survival) signals. 55-57,63,64 Previous studies demonstrate that encapsulated LET nanoparticles, once inside the MDA-MB-231 cells, showed upregulated expression of the proapoptotic genes caspase-3 and caspase-9.<sup>63</sup> The same study showed the downregulation of cyclin-D, cyclin-E, MMP-2, and MMP-9 genes in MDA-MB-231.64 These genes are involved in breast cancer growth and progression.<sup>64</sup> In this work, LET from drug-loaded nano-Ca@BPBPA in MCF-7 cells was expected to follow both pathways, inhibiting the aromatase enzyme and disrupting gene expression such as caspase-3, caspase-9, cyclin-D, cyclin-E, MMP-2, and MMP-9 inside the cell, while in MDA-MB-231, only disruption in the gene expression might be generated, resulting in lower cytotoxicity effects.

The osteoblast hFOB 1.19 cells were treated with LET, empty, and drug-loaded nano-Ca@BPBPA at a concentration range of 6.3-50  $\mu$ M for 24, 48, and 72 h. LET, empty, and drug-loaded nano-Ca@BPBPA were not expected to induce significant cytotoxicity against these cell lines, indicating that these will not cause cytotoxicity effects on the viability of normal cells found in the bone microenvironment. The results demonstrate that nano-Ca@BPBPA and LET did not cause a considerable decrease in the cell viability (%RCV > 93%) at a concentration range of  $6.3-25 \mu M$  after all time points. Furthermore, it was found that, at concentrations of 6.3 and 12.5 μM, drug-loaded nano-Ca@BPBPA did not generate a decrease in the cell viability (%RCV > 93%) in this normal osteoblast cell line (Figure 10i,j). However, at concentrations of 25 and 50 µM, drug-loaded nano-Ca@BPBPA causes a significant decrease in the cell viability after 24 h (%RCV < 59%), 48 h (%RCV < 18%), and 72 h (%RCV < 8%) of

treatment (Figure 10k,l). These results point to the possible development of drug-loaded nano-Ca@BPCPs that might effect higher cytotoxicity than LET on ER-positive (MCF-7) and TNBC breast cancer (MDA-MB-231) cell lines without adversely affecting the normal noncancerous osteoblast cell (hFOB 1.19) at the metastatic site.

#### CONCLUSIONS

Three crystalline phases, namely, BPBPA-Ca, BPBPA-Zn, and BPBPA-Mg, were obtained from the synthesis of BPBPA, the BP analogue of BPDC, with nontoxic metals (Ca<sup>2+</sup>, Zn<sup>2+</sup>, and Mg<sup>2+</sup>). The crystal structures of these materials revealed channels BPBPA-Ca (11 Å  $\times$  12 Å), BPBPA-Zn (10 Å  $\times$  13 Å), and BPBPA-Mg (8 Å  $\times$  11 Å), which enabled the encapsulation of LET, an antineoplastic drug prescribed for ER-positive breast cancer and often combined with commercial BPs for OM therapy, thus allowing the evaluation of these materials as potential bone-targeted DDSs to treat OM. BPBPA-Ca was selected because this framework displayed the highest yield, largest channels, and more drastic pH degradation, potentially enabling maximum delivery of its cargo to the target site, the bone microenvironment. The PITnanoemulsion method was effectively used to reduce the particle size of BPBPA-Ca (~100 µm), leading to nano-Ca@ BPBPA (~160 d. nm). This material retains a monodisperse homogeneous particle size distribution for up to 48 h in 10% FBS/PBS. These results suggest that nano-Ca@BPBPA does not form large aggregates in serumlike media. The binding assays evidence the higher affinity of nano-Ca@BPBPA to HA compared with commercial and other extended BPs [ZOLE (1.7 times),<sup>22</sup> RISE (1.4 times),<sup>23</sup> and BBPA (1.9 times)<sup>24</sup>] after 24 h. These results suggest that nano-Ca@BPBPA might lead to a higher measurable bone affinity compared with commercial BPs, potentiating its use as a bone-targeted DDS. Furthermore, the amounts of LET loaded and released (~20 wt %) from BPBPA and nano-Ca@BPBPA are comparable to those reported for BPDC-based CCs [i.e., UiO-67-(NH<sub>2</sub>)<sub>2</sub> (11 Å), BPDC-Zr ( $\sim$ 12 Å), and bio-MOF-1 (7 and 10 Å)], where antineoplastic drugs, such as pemetrexed and Ru-90, and other pharmaceutical compounds, such as calcein and  $\alpha$ -cyano-4hydroxycinnamic acid, were loaded in PBS (pH = 7.4). Cell viability assays demonstrated that drug-loaded nano-Ca@ BPBPA displays higher cytotoxicity effects against the breast cancer cells MCF-7 (%RCV =  $21 \pm 1\%$ ) and MDA-MB-231 (%RCV = 45  $\pm$  4%) by significantly decreasing the cell viability compared with LET (%RCV =  $70 \pm 1\%$  in MCF-7and 99  $\pm$  1% in MDA-MB-231) at 12.5  $\mu$ M after 72 h. At this concentration, no significant cytotoxicity was found for the hFOB 1.19 cells treated with drug-loaded nano-Ca@BPBPA and LET (%RCV =  $100 \pm 1$ %). Collectively, these results demonstrate the potential of nano-Ca@BPCPs as promising DDSs to treat OM or other bone-related diseases because these materials present measurably higher affinity, allowing bone-targeted drug delivery under acidic environments and effecting the cytotoxicity on ER-positive or TNBC cell lines without significantly affecting the normal osteoblast at the metastatic site.

### ASSOCIATED CONTENT

## Supporting Information

The Supporting Information is available free of charge at https://pubs.acs.org/doi/10.1021/acsami.3c05421.

Complete descriptions for the synthesis and characterization of BPBPA and the BPBPA-based BPCPs by Raman, PXRD, SCXRD, TGA, and SEM-EDS, as well as experimental procedures and data for the calibration curves, dissolution curves, PIT-nanoemulsion synthesis of nano-Ca@BPBPA, aggregation measurements, binding assays, drug loading and release from BPBPA-Ca and nano-Ca@BPBPA, and cytotoxicity assays (PDF)

Crystallographic data for BPBPA-Ca (CIF)

Crystallographic data for BPBPA-Zn (CIF)

Crystallographic data for BPBPA-Mg (CIF)

#### AUTHOR INFORMATION

## **Corresponding Author**

Vilmalí López-Mejías – Department of Chemistry, University of Puerto Rico, San Juan, Puerto Rico 00931, United States; Crystallization Design Institute and the Molecular Sciences Research Center, Inc., University of Puerto Rico, San Juan, Puerto Rico 00931, United States; o orcid.org/0000-0003-2138-8414; Email: vilmali.lopez@upr.edu

#### **Authors**

Lesly Carmona-Sarabia - Department of Chemistry, University of Puerto Rico, San Juan, Puerto Rico 00931, United States; Crystallization Design Institute and the Molecular Sciences Research Center, Inc., University of Puerto Rico, San Juan, Puerto Rico 00931, United States; orcid.org/0000-0002-1733-319X

Gabriel Quiñones Vélez - Department of Chemistry, University of Puerto Rico, San Juan, Puerto Rico 00931, United States; Crystallization Design Institute and the Molecular Sciences Research Center, Inc., University of Puerto Rico, San Juan, Puerto Rico 00931, United States; orcid.org/0000-0001-8789-1616

Darilys Mojica-Vázquez - Department of Chemistry, University of Puerto Rico, San Juan, Puerto Rico 00931, United States; Crystallization Design Institute and the Molecular Sciences Research Center, Inc., University of Puerto Rico, San Juan, Puerto Rico 00931, United States; orcid.org/0000-0003-4062-9703

Andrea M. Escalera-Joy – Department of Chemistry, University of Puerto Rico, San Juan, Puerto Rico 00931, United States; Crystallization Design Institute and the Molecular Sciences Research Center, Inc., University of Puerto Rico, San Juan, Puerto Rico 00931, United States; orcid.org/0000-0002-2907-2636

Solimar Esteves-Vega - Crystallization Design Institute and the Molecular Sciences Research Center, Inc., University of Puerto Rico, San Juan, Puerto Rico 00931, United States; Interdisciplinary Sciences Program, University of Puerto Rico, San Juan, Puerto Rico 00931, United States; o orcid.org/ 0000-0002-0035-826X

Esther A. Peterson-Peguero – Department of Biology, University of Puerto Rico, San Juan, Puerto Rico 00931, United States; orcid.org/0000-0001-7497-0980

Complete contact information is available at: https://pubs.acs.org/10.1021/acsami.3c05421

## **Author Contributions**

L.C.-S., E.A.P.-P., and V.L.-M. designed the research. L.C.-S., G.Q.-V., D.M.-V., A.M.E.-J., and S.E.-V. performed the synthesis and characterization and the experimental procedures

for the dissolution curves, PIT-nanoemulsion synthesis, aggregation measurements, binding assays, drug loading and release, and in vitro experiments under the supervision of E.A.P.-P. and V.L.-M. The manuscript was written by L.C.-S. and V.L.-M. with contribution from all authors. All authors have given approval to the final version of the manuscript.

#### **Funding**

This research was supported by the National Institutes of Health (NIH) under Grant 1SC2GM127223-01A1 and the Institutional Research Funds of the University of Puerto Rico, Rio Piedras (FIPI Funds 2017-2019 and 2019-2021). The Rigaku XtaLAB SuperNova single-crystal X-ray microdiffractometer was acquired through the Major Research Instrumentation Program (CHE-1626103) of the NSF. The thermogravimetric analyzer (TA Instruments, Inc.) was purchased with start-up funds from the Puerto Rico Institute for Functional Nanomaterials (EPS-100241). The NSF's ChemMatCARS, Sector 15, at the APS, ANL, is supported by the Divisions of Chemistry (CHE) and Materials Research (DMR), NSF, under Grant NSF/CHE-1834750. This research used resources of the APS, a U.S. Department of Energy (DOE), Office of Science, user facility operated for the DOE, Office of Science, by ANL under Contract DE-AC02-06CH11357.

#### Notes

The authors declare no competing financial interest.

### ACKNOWLEDGMENTS

We thank the Material Characterization Center for technical support during collection of the SEM-EDS data.

#### REFERENCES

- (1) Rucci, N.; Ricevuto, E.; Ficorella, C.; Longo, M.; Perez, M.; Di Giacinto, C.; Funari, A.; Teti, A.; Migliaccio, S. In Vivo Bone Metastases, Osteoclastogenic Ability, and Phenotypic Characterization of Human Breast Cancer Cells. *Bone* **2004**, *34* (4), *697*–709.
- (2) Spinello, A.; Martini, S.; Berti, F.; Pennati, M.; Pavlin, M.; Sgrignani, J.; Grazioso, G.; Colombo, G.; Zaffaroni, N.; Magistrato, A. Rational Design of Allosteric Modulators of the Aromatase Enzyme: An Unprecedented Therapeutic Strategy to Fight Breast Cancer. *Eur. J. Med. Chem.* **2019**, *168*, 253–262.
- (3) Siegel, R. L.; Miller, K. D.; Fuchs, H. E.; Jemal, A. Cancer Statistics, 2022. *CA. Cancer J. Clin.* **2022**, 72 (1), 7–33.
- (4) Harborg, S.; Zachariae, R.; Olsen, J.; Johannsen, M.; Cronin-Fenton, D.; Bøggild, H.; Borgquist, S. Overweight and Prognosis in Triple-Negative Breast Cancer Patients: A Systematic Review and Meta-Analysis. *npj Breast Cancer* **2021**, *7* (1), 119–127.
- (5) Chen, Y. C.; Sosnoski, D. M.; Mastro, A. M. Breast Cancer Metastasis to the Bone: Mechanisms of Bone Loss. *Breast Cancer Res.* **2010**, *12* (6), 215–225.
- (6) Holen, I.; Coleman, R. E. Bisphosphonates as Treatment of Bone Metastases. *CPD* **2010**, *16*, 1262–1271.
- (7) Marazzi, F.; Orlandi, A.; Manfrida, S.; Masiello, V.; Di Leone, A.; Massaccesi, M.; Moschella, F.; Franceschini, G.; Bria, E.; Gambacorta, M. A.; Masetti, R.; Tortora, G.; Valentini, V. Diagnosis and Treatment of Bone Metastases in Breast Cancer: Radiotherapy, Local Approach and Systemic Therapy in a Guide for Clinicians. *Cancers (Basel)*. **2020**, *12* (9), 2390.
- (8) Lin, Y.; Villacanas, M. G.; Zou, H.; Liu, H.; Carcedo, I. G.; Wu, Y.; Sun, B.; Wu, X.; Prasadam, I.; Monteiro, M. J.; Li, L.; Xu, Z. P.; Gu, W. Calcium-Bisphosphonate Nanoparticle Platform as a Prolonged Nanodrug and Bone-Targeted Delivery System for Bone Diseases and Cancers. ACS Appl. Bio Mater. 2021, 4 (3), 2490–2501. (9) Ma, S.; Goh, E. L.; Jin, A.; Bhattacharya, R.; Boughton, O. R.;
- Patel, B.; Karunaratne, A.; Vo, N. T.; Atwood, R.; Cobb, J. P.; Hansen, U.; Abel, R. L. Long-Term Effects of Bisphosphonate Therapy:

- Perforations, Microcracks and Mechanical Properties. Sci. Rep. 2017, 7 (1), 1–10.
- (10) Nogués, X.; Martinez-Laguna, D. Update on Osteoporosis Treatment. *Med. Clin. (Barc).* **2018**, *150* (12), 479–486.
- (11) Orellana-Tavra, C.; Marshall, R. J.; Baxter, E. F.; Lázaro, I. A.; Tao, A.; Cheetham, A. K.; Forgan, R. S.; Fairen-Jimenez, D. Drug Delivery and Controlled Release from Biocompatible Metal-Organic Frameworks Using Mechanical Amorphization. *J. Mater. Chem. B* **2016**, *4* (47), 7697–7707.
- (12) Orellana-Tavra, C.; Köppen, M.; Li, A.; Stock, N.; Fairen-Jimenez, D. Biocompatible, Crystalline, and Amorphous Bismuth-Based Metal-Organic Frameworks for Drug Delivery. *ACS Appl. Mater. Interfaces* **2020**, *12* (5), 5633–5641.
- (13) Rojas, S.; Horcajada, P. Understanding the Incorporation and Release of Salicylic Acid in Metal-Organic Frameworks for Topical Administration. *Eur. J. Inorg. Chem.* **2021**, *14*, 1325–1331.
- (14) Sun, Y.; Zheng, L.; Yang, Y.; Qian, X.; Fu, T.; Li, X.; Yang, Z.; Yan, H.; Cui, C.; Tan, W. Metal-Organic Framework Nanocarriers for Drug Delivery in Biomedical Applications. *Nano-Micro Lett.* **2020**, *12* (1). DOI: 10.1007/s40820-020-00423-3
- (15) Suresh, K.; López-Mejías, V.; Roy, S.; Camacho, D. F.; Matzger, A. J. Leveraging Framework Instability: A Journey from Energy Storage to Drug Delivery. *Synlett* **2020**, *31* (16), 1573–1580.
- (16) Cai, W.; Wang, J.; Chu, C.; Chen, W.; Wu, C.; Liu, G. Metal-Organic Framework-Based Stimuli-Responsive Systems for Drug Delivery. *Adv. Sci.* **2019**, *6* (1), 1801526.
- (17) Rodrigues, N. M.; Martins, J. B. L. Theoretical Evaluation of the Performance of IRMOFs and M-MOF-74 in the Formation of 5-Fluorouracil@MOF. RSC Adv. 2021, 11 (49), 31090–31097.
- (18) Liu, W.; Pan, Y.; Zhong, Y.; Li, B.; Ding, Q.; Xu, H.; Qiu, Y.; Ren, F.; Li, B.; Muddassir, M.; Liu, J. A Multifunctional Aminated UiO-67 Metal-Organic Framework for Enhancing Antitumor Cytotoxicity through Bimodal Drug Delivery. *Chem. Eng. J.* **2021**, 412, 127899.
- (19) Gandara-Loe, J.; Ortuno-Lizarán, I.; Fernández-Sanchez, L.; Alió, J. L.; Cuenca, N.; Vega-Estrada, A.; Silvestre-Albero, J. Metal-Organic Frameworks as Drug Delivery Platforms for Ocular Therapeutics. ACS Appl. Mater. Interfaces 2019, 11 (2), 1924–1931.
- (20) Marson Armando, R. A.; Abuçafy, M. P.; Graminha, A. E.; Silva, R. S. da; Frem, R. C. G. Ru-90@bio-MOF-1: A Ruthenium(II) Metallodrug Occluded in Porous Zn-Based MOF as a Strategy to Develop Anticancer Agents. *J. Solid State Chem.* **2021**, 297, 122081.
- (21) Quinones Vélez, G.; Carmona-Sarabia, L.; Rodríguez-Silva, W. A.; Rivera Raíces, A. A.; Feliciano Cruz, L.; Hu, T.; Peterson, E.; López-Mejiás, V. Potentiating Bisphosphonate-Based Coordination Complexes to Treat Osteolytic Metastases. *J. Mater. Chem. B* **2020**, 8 (10), 2155–2168.
- (22) Quiñones Vélez, G.; Carmona-Sarabia, L.; Rivera Raíces, A. A.; Hu, T.; Peterson-Peguero, E. A.; López-Mejías, V. High Affinity Zoledronate-Based Metal Complex Nanocrystals to Potentially Treat Osteolytic Metastases. *Mater. Adv.* **2022**, *3* (7), 3251–3266.
- (23) Quiñones Vélez, G.; Carmona-Sarabia, L.; Santiago, A. P.; Figueroa Guzmán, A.; Hu, C.; Peterson-peguero, E.; López-Mejías, V. Beyond Antiresorptive Activity: Risedronate-Based Coordination Complexes To Potentially Treat Osteolytic Metastases. ACS Appl. Bio Mater. 2023, 6, 973–986.
- (24) Carmona-Sarabia, L.; Quiñones Vélez, G.; Escalera-Joy, A. M.; Mojica-Vázquz, D.; Esteves-Vega, S.; Peterson-Peguero, E. A.; López-Mejías, V. Design of Extended Bisphosphonate-based Coordination polymers as Bone-Targeted Drug Delivery Systems for Breast Cancer Induced Osteolytic Metastasis and Other Bone Therapies. *Inorg. Chem.* **2023**, *62*, 9440–9453.
- (25) Kennel, K. A.; Drake, M. T. Adverse Effects of Bisphosphonates: Implications for Osteoporosis Management. *Mayo Clin. Proc.* **2009**, 84 (7), 632–638.
- (26) Yamaguchi, M. Role of Nutritional Zinc in the Prevention of Osteoporosis. *Mol. Cell. Biochem.* **2010**, 338 (1–2), 241–254.

- (27) Castiglioni, S.; Cazzaniga, A.; Albisetti, W.; Maier, J. A. M. Magnesium and Osteoporosis: Current State of Knowledge and Future Research Directions. *Nutrients* **2013**, *5* (8), 3022–3033.
- (28) Lecouvey, M.; Mallard, I.; Bailly, T.; Burgada, R.; Leroux, Y. A Mild and Efficient One-Pot Synthesis of 1-Hydroxymethylene-1,1-Bisphosphonic Acids. Preparation of New Tripod Ligands. *Tetrahedron Lett.* **2001**, 42 (48), 8475–8478.
- (29) Guenin, E.; Degache, E.; Liquier, J.; Lecouvey, M. Synthesis of 1-Hydroxymethylene-1,1-Bis(Phosphonic Acids) from Acid Anhydrides: Preparation of a New Cyclic 1-Acyloxymethylene-1,1-Bis(Phosphonic Acid). *Eur. J. Org. Chem.* **2004**, *14*, 2983–2987.
- (30) Guenin, E.; Ledoux, D.; Oudar, O.; Lecouvey, M.; Kraemer, M. Structure-Activity Relationships of a New Class of Aromatic Bisphosphonates That Inhibit Tumor Cell Proliferation in Vitro. *Anticancer Res.* **2005**, *25* (2A), 1139–1145.
- (31) Egorov, M.; Aoun, S.; Padrines, M.; Redini, F.; Heymann, D.; Lebreton, J.; Mathé-Allainmat, M. A One-Pot Synthesis of 1-Hydroxy-1,1-Bis(Phosphonic Acid)s Starting from the Corresponding Carboxylic Acids. *Eur. J. Org. Chem.* **2011**, *35*, 7148–7154.
- (32) Burdett, J. K.; Hoffmann, R.; Fay, R. C. Eight-Coordination. *Inorg. Chem.* 1978, 17 (9), 2553–2568.
- (33) Firor, R. L.; Seff, K. Seven-Coordinate Distorted C3v-Capped Trigonal-Prismatic Europium(II). Crystal Structure of Hydrated Europium(II)-Exchanged Sodium Zeolite A, Eu5Na2-A. *Inorg. Chem.* 1978, 17 (8), 2144–2148.
- (34) Uchtman, V. A. Structural investigations of calcium binding molecules. II. Crystal and molecular structures of calcium dihydrogen ethane-1-hydroxy-1,1-diphosphonate dihydrate, CaC(CH<sub>3</sub>)(OH)-(PO<sub>3</sub>H)<sub>2</sub>·2H<sub>2</sub>O. Implications for polynuclear complex formation. *J. Phys. Chem.* **1972**, *76*, 1304–1310.
- (35) Stavgianoudaki, N.; Papathanasiou, K. E.; Colodrero, R. M. P.; Choquesillo-Lazarte, D.; Garcia-Ruiz, J. M.; Cabeza, A.; Aranda, M. A. G.; Demadis, K. D. Crystal Engineering in Confined Spaces. A Novel Method to Grow Crystalline Metal Phosphonates in Alginate Gel Systems. *CrystEngComm* **2012**, *14* (17), 5385–5389.
- (36) Liu, D.; Kramer, S. A.; Huxford-Phillips, R. C.; Wang, S.; Della Rocca, J.; Lin, W. Coercing Bisphosphonates to Kill Cancer Cells with Nanoscale Coordination Polymers. *Chem. Commun.* **2012**, *48* (21), 2668–2670.
- (37) Vassaki, M.; Papathanasiou, K. E.; Hadjicharalambous, C.; Chandrinou, D.; Turhanen, P.; Choquesillo-Lazarte, D.; Demadis, K. D. Self-Sacrificial MOFs for Ultra-Long Controlled Release of Bisphosphonate Anti-Osteoporotic Drugs. *Chem. Commun.* **2020**, *56* (38), 5166–5169.
- (38) Patel, K.; Kumar, A.; Durani, S. Analysis of the Structural Consensus of the Zinc Coordination Centers of Metalloprotein Structures. *Biochim. Biophys. Acta Proteins Proteomics* **2007**, 1774 (10), 1247–1253.
- (39) Fu, R.; Hu, S.; Wu, X. Luminescent Zinc Phosphonates for Ratiometric Sensing of 2,4,6-Trinitrophenol and Temperature. *Cryst. Growth Des.* **2016**, *16* (9), 5074–5083.
- (40) Zhang, X. L.; Cheng, K.; Wang, F.; Zhang, J. Chiral and Achiral Imidazole-Linked Tetrahedral Zinc Phosphonate Frameworks with Photoluminescent Properties. *J. Chem. Soc. Dalt. Trans.* **2014**, 43 (1), 285–289.
- (41) Adrian-Scotto, M.; Mallet, G.; Vasilescu, D. Hydration of Mg++: A Quantum DFT and Ab Initio HF Study. *J. Mol. Struct. THEOCHEM* **2005**, 728, 231–242.
- (42) Imhof, P.; Noe, F.; Fischer, S.; Smith, J. C. AM1/d Parameters for Magnesium in Metalloenzymes. *J. Chem. Theory Comput.* **2006**, 2 (4), 1050–1056.
- (43) Li, Q.; Zheng, J.; Tan, H.; Li, X.; Chen, G.; Jia, Z. Unique Kinase Catalytic Mechanism of AceK with a Single Magnesium Ion. *PLoS One* **2013**, *8* (8), e72048.
- (44) Ma, K. R.; Zhang, Y.; Kan, Y. H.; Yang, X. J.; Cong, M. H. Three M(II)-Diphosphonate Coordination Polymers with N-Heterocyclic Group (M = Ni, Fe, Mg): Synthesis, Characterization and Magnetic Properties. *Synth. Met.* **2013**, *182*, 40–48.

- (45) Senthil Raja, D.; Lin, P. C.; Liu, W. R.; Zhan, J. X.; Fu, X. Y.; Lin, C. H. Multidimensional (0D to 3D) Alkaline-Earth Metal Diphosphonates: Synthesis, Structural Diversity, and Luminescence Properties. *Inorg. Chem.* **2015**, *54* (9), 4268–4278.
- (46) Jiang, Z.; Wang, T.; Yuan, S.; Wang, M.; Qi, W.; Su, R.; He, Z. A Tumor-Sensitive Biological Metal-Organic Complex for Drug Delivery and Cancer Therapy. *J. Mater. Chem. B* **2020**, 8 (32), 7189–7196.
- (47) Rezić, I. Nanoparticles for Biomedical Application and Their Synthesis. *Polymers (Basel)*. **2022**, *14* (22), 4961–4980.
- (48) Lima, A. C.; Alvarez-Lorenzo, C.; Mano, J. F. Design Advances in Particulate Systems for Biomedical Applications. *Adv. Healthc. Mater.* **2016**, 5 (14), 1687–1723.
- (49) Giger, E. V.; Castagner, B.; Leroux, J. C. Biomedical Applications of Bisphosphonates. *J. Controlled Release* **2013**, *167* (2), 175–188.
- (50) Sun, S.; Tao, J.; Sedghizadeh, P. P.; Cherian, P.; Junka, A. F.; Sodagar, E.; Xing, L.; Boeckman, R. K.; Srinivasan, V.; Yao, Z.; Boyce, B. F.; Lipe, B.; Neighbors, J. D.; Russell, G. G.; McKenna, C. E.; Ebetino, F. H. Bisphosphonates for Delivering Drugs to Bone. *Br. J. Pharmacol.* **2021**, *178* (9), 2008–2025.
- (51) Shah, A.; Bloomquist, E.; Tang, S.; Fu, W.; Bi, Y.; Liu, Q.; Yu, J.; Zhao, P.; Palmby, T. R.; Goldberg, K. B.; Chang, G.; Patel, P.; Alebachew, E.; Tilley, A.; Pierce, W.; Ibrahim, A.; Blumenthal, G. M.; Sridhara, R.; Beaver, J. A.; Pazdur, R. FDA Approval: Ribociclib for the Treatment of Postmenopausal Women with Hormone Receptor-Positive, HER2-Negative Advanced or Metastatic Breast Cancer. Clin. Cancer Res. 2018, 24 (13), 2999.
- (52) Sun, J.; Wei, Q.; Zhou, Y.; Wang, J.; Liu, Q.; Xu, H. A Systematic Analysis of FDA-Approved Anticancer Drugs. *BMC Syst. Biol.* **2017**, *11*, 27–102.
- (53) Wong, M. H.; Pavlakis, N. Optimal Management of Bone Metastases in Breast Cancer Patients. *Breast Cancer Targets Ther.* **2011**, *3*, 35–60.
- (54) Ripamonti, C.; Trippa, F.; Barone, G.; Maranzano, E. Prevention and Treatment of Bone Metastases in Breast Cancer. *J. Clin. Med.* **2013**, 2 (3), 151–175.
- (55) Wang, M.; Xia, F.; Wei, Y.; Wei, X. Molecular Mechanisms and Clinical Management of Cancer Bone Metastasis. *Bone Res.* **2020**, 8 (1), 30–50.
- (56) Lau, Y. S.; Danks, L.; Sun, S. G.; Fox, S.; Sabokbar, A.; Harris, A.; Athanasou, N. A. RANKL-Dependent and RANKL-Independent Mechanisms of Macrophage-Osteoclast Differentiation in Breast Cancer. *Breast Cancer Res. Treat.* **2007**, *105* (1), 7–16.
- (57) Kang, H.; Xiao, X.; Huang, C.; Yuan, Y.; Tang, D.; Dai, X.; Zeng, X. Potent Aromatase Inhibitors and Molecular Mechanism of Inhibitory Action. *Eur. J. Med. Chem.* **2018**, *143*, 426–437.
- (58) Hernando, C.; Ortega-Morillo, B.; Tapia, M.; Moragón, S.; Martínez, M. T.; Eroles, P.; Garrido-Cano, I.; Adam-Artigues, A.; Lluch, A.; Bermejo, B.; Cejalvo, J. M. Oral Selective Estrogen Receptor Degraders (Serds) as a Novel Breast Cancer Therapy: Present and Future from a Clinical Perspective. *Int. J. Mol. Sci.* **2021**, 22 (15), 7812–7833.
- (59) Croset, M.; Clézardin, P. MicroRNA-Mediated Regulation of Bone Metastasis Formation: From Primary Tumors to Skeleton. *Bone Cancer* **2015**, 479–490.
- (60) Welsh, J. E. Animal Models for Studying Prevention and Treatment of Breast Cancer. *Anim. Model. Study Hum. Dis.* **2013**, 997–1018.
- (61) Harris, S. A.; Enger, R. J.; Riggs, L. B.; Spelsberg, T. C. Development and Characterization of a Conditionally Immortalized Human Fetal Osteoblastic Cell Line. *J. Bone Miner. Res.* **1995**, *10* (2), 178–186.
- (62) Almutairi, M. S.; Al Suwayyid, A. N.; Aldarwesh, A.; Aboulwafa, O. M.; Attia, M. I. Antiestrogenic Activity and Possible Mode of Action of Certain New Nonsteroidal Coumarin-4-Acetamides. *Molecules* **2020**, 25 (7), 1553.
- (63) Ahmadi, S.; Seraj, M.; Chiani, M.; Hosseini, S.; Bazzazan, S.; Akbarzadeh, I.; Saffar, S.; Mostafavi, E. In Vitro Development of

Controlled-Release Nanoniosomes for Improved Delivery and Anticancer Activity of Letrozole for Breast Cancer Treatment. Int. J. Nanomedicine 2022, 17, 6233-6255.

(64) Sahrayi, H.; Hosseini, E.; Karimifard, S.; Khayam, N.; Meybodi, S. M.; Amiri, S.; Bourbour, M.; Farasati far, B.; Akbarzadeh, I.; Bhia, M.; Hoskins, C.; Chaiyasut, C. Co-Delivery of Letrozole and Cyclophosphamide via Folic Acid-Decorated Nanoniosomes for Breast Cancer Therapy: Synergic Effect, Augmentation of Cytotoxicity, and Apoptosis Gene Expression. Pharmaceuticals 2022, 15, 6-25.

## **Recommended by ACS**

**Design of Extended Bisphosphonate-Based Coordination** Polymers as Bone-Targeted Drug Delivery Systems for Breast Cancer-Induced Osteolytic Metastasis and Other...

Lesly Carmona-Sarabia, Vilmalí López-Mejías, et al.

JUNE 06, 2023

INORGANIC CHEMISTRY

READ 🗹

Thiophene-Derived Schiff Base Complexes: Synthesis, Characterization, Antimicrobial Properties, and Molecular **Docking** 

Saira Nayab, Hyosun Lee, et al.

MAY 12, 2023

ACS OMEGA

READ

In Vitro and In Vivo Biological Activities of Dipicolinate Oxovanadium(IV) Complexes

Katarzyna Choroba, Alexandra R. Fernandes, et al.

JUNE 13, 2023

JOURNAL OF MEDICINAL CHEMISTRY

READ 🗹

A Series of Non-Oxido  $V^{\scriptscriptstyle{IV}}$  Complexes of Dibasic ONS Donor Ligands: Solution Stability, Chemical Transformations, Protein Interactions, and Antiproliferati...

Atanu Banerjee, Rupam Dinda, et al.

MAY 08, 2023

INORGANIC CHEMISTRY

READ 🗹

Get More Suggestions >